ABSTRACT

Title of dissertation: ON THE NATURE OF THE JOSEPHSON EFFECT IN TOPOLOGICALLY NONTRIVIAL MATERIALS

Christie Jordan Trimble
Doctor of Philosophy, 2021

Dissertation directed by: Professor James R. Williams
Department of Physics

A Josephson junction (JJ) couples the supercurrent flowing between two weakly linked superconductors to the phase difference between them via a tunnel barrier, giving rise to a current-phase relation (CPR). While a sinusoidal CPR is expected for conventional junctions with insulating weak links, devices made from some exotic materials may give rise to unconventional CPRs and unusual Josephson effects. Here, I experimentally investigate three such cases.

In the first part of the thesis, I fabricate JJs with weak links made of the topological crystalline insulator $Pb_{0.5}Sn_{0.5}Te$ and compare them with JJs made from its topologically trivial cousin, PbTe. I find that measurements of the AC Josephson effect reveal a stark difference between the two: while the PbTe JJs exhibit Shapiro steps at the expected values of $V = nhf/2e$, $Pb_{0.5}Sn_{0.5}Te$ JJs show more complicated subharmonic structure. I present the skewed sinusoidal CPR necessary to reproduce these measurements and discuss a potential origin for this alteration.

Next, I investigate the proximity-induced superconductivity in SnTe nanowires

by incorporating them as weak links in Josephson junctions. I report indications of an unexpected breaking of time-reversal symmetry in these devices, including observations of an asymmetric critical current in the DC Josephson effect, a prominent second harmonic in the AC Josephson effect, and a magnetic diffraction pattern with a minimum in critical current at zero magnetic field. I analyze how multiband effects and the experimentally visualized ferroelectric domain walls may give rise to a nonstandard CPR in the junction.

Finally, I measure JJs with weak links made of the topological insulator $(BiSb)_2Te_3$. Under low frequency RF radiation, I observe suppression of the first and third Shapiro steps, consistent with the fractional AC Josephson effect. This could indicate a 4π periodic component in the junction's CPR, potentially implying the presence of Majorana bound states. However, not all of the devices showed this behavior; some devices show suppression of only the first step, while others show distortions to the AC Josephson effect which differ upon repeated measurements, possibly indicating other nonequilibrium effects at play. I discuss this behavior and possible topologically trivial sources of step suppression found in the literature.

ON THE NATURE OF THE JOSEPHSON EFFECT IN TOPOLOGICALLY NONTRIVIAL MATERIALS

by

Christie Jordan Trimble

Dissertation submitted to the Faculty of the Graduate School of the
University of Maryland, College Park in partial fulfillment
of the requirements for the degree of
Doctor of Philosophy
2021

Advisory Committee:
Professor James R. Williams, Chair/Advisor
Professor Alicia J. Kollár
Professor Johnpierre Paglione
Professor Ichiro Takeuchi
Professor Frederick C. Wellstood

Dedication

For Jake: my husband, my tireless advocate, and my best friend.

Acknowledgments

I offer my utmost gratitude to my family for their unwavering support and love during this season of my life. It has been truly comforting to know that you are always on my side.

To Jimmy: it has been a pleasure to learn physics from you. You have created a group of excellent scientists, and I count myself lucky to have been a part of your lab's success. Although your guidance and wisdom have taught me much over the years, the best gift you have given me is your belief in me, especially when I did not believe in myself. You stood by me in my failings and ushered me forward to today, and for this I will always be grateful.

I am indebted to Judy Cha and Pengzi Liu for their synthesis of exceptional materials and for working with me to study them. I thank Ming Tso-Wei and Sandesh Kalantre for their brilliance in computational modeling which contributed greatly to my projects. A huge thanks goes to Ilan Rosen and David Goldhaber-Gordon for their collaborations, and for granting me the opportunity to measure their new and exciting devices. I give further thanks to Ilan for the inspiration of his work, which has helped me to feel less alone as a senior graduate student in our niche subfield.

To my lab group, I cannot thank you enough for the support you've given me throughout my years here. Working with such exceptional scientists has benefited my research and enabled me to persevere through the many challenges of doing science. My utmost thanks goes to Rodney Snyder for his patience and guidance in teaching me when I first arrived in graduate school, and for mentoring me in the years that followed. To Sam, Sungha, Sandesh, Ming, Ray, Steven, and Julia, your companionship and scientific excellence were invaluable to me during this time. I especially want to thank Sandesh for picking me up off the floor when I was down.

I am grateful for the support I received from the Joint Quantum Institute and the NSF. To my dissertation committee I extend my sincere thanks for aiding me in this final step. I also thank Anna Zaniewski and Robert Nemanich, who set me on the path I walk today. Lastly, I am grateful to the staff at the Nanocenter FabLab, to Dave Myers, and to Doug Benson for their excellence in technical support.

Table of Contents

List of Figures

List of Abbreviations

ABS	Andreev bound states
BST	Bismuth Antimony Telluride (BiSbTe)
BTRS	Broken time-reversal symmetry
BCS	Bardeen, Cooper, and Schrieffer theory
CPR	Current-phase relation
EBL	Electron beam lithography
GL	Ginzburg-Landau
I_c	Critical current
IPA	Isopropyl alcohol
JJ	Josephson junction
KPFM	Kelvin probe force microscopy
LZT	Landau-Zener transition
MBE	Molecular beam epitaxy
MDP	Magnetic diffraction pattern
m_e	Mass of an electron
PMMA	Poly(methyl methacrylate)
RCSJ	Resistively and capacitively shunted junction model
RF	Radio frequency
RSJ	Resistively shunted junction model
SEM	Scanning electron microscope

T_c	Critical temperature
TCI	Topological Crystalline Insulator
TEM	Transmission electron microscope
TI	Topological Insulator

Chapter 1: Introduction

1.1 Superconductivity

The phenomenon of superconductivity was discovered in 1911 by H. K. Onnes, who observed a vanishing electrical resistance in mercury when it was cooled below 4K [1, 2]. This state of zero resistivity below a critical temperature T_c would be discovered in 30+ chemical elements and in hundreds of alloys and compounds over the next century.

Superconductors are more than a stunning display of zero resistance. For comparison, consider the theoretical behavior of electrons in a perfect conductor in the presence of a time varying magnetic field. In this system, electrons must obey $-e\mathbf{E} = m_e\dot{\mathbf{v}} = m_e\dot{\mathbf{J}}/ne$, where m_e is the electron mass, $-e$ is the electron charge, and n is the number density of superconducting carriers. Equivalently,

$$\mathbf{E} = \lambda^2\dot{\mathbf{J}}, \text{ where } \lambda^2 = \frac{m_e}{ne^2}; \tag{1.1}$$

applying Faraday's law, this becomes

$$\boldsymbol{\nabla} \times \dot{\mathbf{J}} = -\frac{ne^2}{m_e}\dot{\mathbf{B}}. \tag{1.2}$$

Using the Ampere-Maxwell law and vector identities, and neglecting the displacement current, we can transform Eq. 1.1 to read $\nabla^2\dot{\mathbf{B}} = \dot{\mathbf{B}}/\lambda^2$, which has the solution $\dot{\mathbf{B}}(z) = \dot{\mathbf{B}}(0)e^{-z/\lambda}$. Hence, $\dot{\mathbf{B}}$ decreases exponentially with distance z into the material, leaving a constant $\mathbf{B}$ below a characteristic penetration depth λ. If a material that is subject to an external $\mathbf{B}$ transitions to become a perfect conductor, the field will be frozen inside and cannot be changed.

Yet, this is not the case for superconductors. In 1933 Meissner and Ochsenfeld demonstrated that instead, B goes to zero inside a superconductor [3, 4]. This phenomenon, termed the *Meissner effect*, involves the expulsion of magnetic field lines from the interior of a material as it transitions to the superconducting state.

The Meissner effect was described phenonemologically by the London brothers in 1935 [5]. In order for Maxwell's equations to yield the Meissner effect, they replaced Eq. 1.2 for a perfect conductor with the relation

$$\boldsymbol{\nabla} \times \mathbf{J} = -\frac{ne^2}{m_e}\mathbf{B}. \tag{1.3}$$

If we proceed mathematically in the same way as before, we now find that

$$\nabla^2\mathbf{B} = -\frac{1}{\lambda_L}\mathbf{B}, \text{ where } {\lambda_L}^2 = \frac{m_e}{\mu_0 ne^2}. \tag{1.4}$$

This has the solution $\mathbf{B}(z) = \mathbf{B}(0)e^{-z/\lambda_L}$ and gives the exponential decay of magnetic fields in the interior of a superconductor. This decay is characterized by the penetration depth, which the Londons estimated to be on the order of 10^{-7}m. It varies between materials and depends on temperature. As expected, for depths significantly beyond λ_L, $\mathbf{B}$ approaches zero, in agreement with the Meissner effect.

With the particular gauge choice such that $\nabla \cdot \mathbf{A} = 0$, Eqs. 1.4 and 1.3 can be combined into a single "London Equation" which relates the supercurrent density to the magnetic vector potential:

$$\mathbf{J} = -\frac{ne^2}{m_e}\mathbf{A}. \tag{1.5}$$

The Londons concluded that "in contrast to the customary conception that in a supraconductor [sic] a current may persist without being maintained by an electric or magnetic field, the current is characterized as a kind of diamagnetic volume current, the existence of which is necessarily dependent upon the presence of a magnetic field." [6]. In other words, *perfect diamagnetism* is a fundamental property of superconductors. Indeed, it is more fundamental than perfect conductivity, which does not explain the Meissner effect.

Although the London equations form a useful framework for describing the behavior of superconductors in electromagnetic fields, they do not provide a microscopic explanation of the phenomenon. In imagining a path toward such a theory, the authors remarked, "suppose the electrons to be coupled by some form of interaction. Then the lowest state of the electrons may be separated by a finite distance from the excited ones" [5]. This was a remarkable insight, but the nature of this interaction would remain unknown for the next two decades.

The mechanism of electronic coupling (for conventional superconductors) was finally elucidated by Bardeen, Cooper, and Schrieffer (BCS) in 1957 [7]. They proposed a small, phonon-mediated attractive potential between electrons near the Fermi surface, causing them to bind together into "Cooper pairs" of two electrons with opposite spin and momentum [8]. Since *pairs* of electrons are bosons, these Cooper pairs are able to condense into the same lowest energy state–the BCS ground state–which is separated from the excited states by energy gap 2Δ. The London equations follow naturally from this formulation.

BCS theory provided a compelling picture of superconductivity as a macroscopic quantum phenomenon. Since they occupy the same ground state, electron pairs in the condensate are characterized by a rigid macroscopic wavefunction which is insensitive to flaws in the lattice, thus realizing perfect conductivity. Above T_c, thermal breakup of the Cooper pairs returns the material to the normal state.

A more comprehensive discussion of BCS theory can be found in Refs. [9–11]. The BCS theory was remarkably successful in describing superconductivity in metals, and its authors received the Nobel Prize in 1972. But phonon-mediated pairing was shown to be not the only type of pairing mechanism when superconductivity at high temperatures was discovered in the 1980s. The pairing mechanisms in these complex materials are still unclear, and today we regard superconductors which do not conform to a phonon-mediated pairing model as "unconventional."

Superconductors may further be characterized as type I or type II. In the former, an external magnetic field is screened entirely (on the scale of the London penetration depth) from the interior of a bulk superconductor until a critical field is reached and the material abruptly enters the normal state. In type II superconductors, above a lower critical field H_{c1}, there exists a mixed state where the field may partially penetrate the superconductor, complicating the phase diagram. Only above an upper critical field H_{c2} does the material transition fully to the normal state. I should note at this point that I use conventional, type I superconductors to build the devices used in my research, so henceforth I will focus my discussion on these.

In the remainder of this section, I briefly discuss the Ginzburg-Landau (GL) formulation [12], which approaches superconductivity through Landau's theory of second order phase transitions. Gorkov showed that the Ginzburg-Landau model can be derived from BCS theory [13] after making suitable approximations. The GL equations are useful for understanding many experimental phenomena, particularly Josephson junctions (JJs) and macroscopic order. The quantity of interest is the complex order parameter $\mathbf{\Psi}(\mathbf{r}) = \Psi_0(\mathbf{r})e^{i\varphi(\mathbf{r})}$, interpreted as the superconducting wavefunction, which should be nonzero below T_c and zero above T_c. GL assumed the existence of a functional $F[\mathbf{\Psi}(\mathbf{r})]$ that gives the difference in free energy between the normal and superconducting states. Near T_c (where the order parameter vanishes) the Ginzburg-Landau free energy should obey an expansion of the form

$$F(\mathbf{\Psi}, \mathbf{\Psi}^*, \mathbf{A}) = \alpha|\mathbf{\Psi}|^2 + \frac{\beta}{2}|\mathbf{\Psi}|^4 + \frac{1}{4m^*}\left|\left(-i\hbar\mathbf{\nabla} + 2e^*\mathbf{A}\right)\mathbf{\Psi}\right|^2 + \frac{B^2}{8\pi}, \tag{1.6}$$

where m^* and e^* are the mass and charge, respectively, of the superconducting carriers, B is the magnetic field, and $\mathbf{A}$ is the vector potential. This free energy can be best understood as representing a charged Bose superfluid whose fundamental components are Cooper pairs (i.e., $e^* = 2e$ and $m^* = 2m_e$). The vector potential $\mathbf{A}$ in the functional couples the charge of the pairs to the electromagnetic field. The final term is the energy of the magnetic field. By minimizing F with respect to $\mathbf{A}$ and using $\boldsymbol{\nabla} \times \mathbf{B} = \mu_0 \mathbf{J}$, one can find that the supercurrent density is characterized by

$$\mathbf{J} = \frac{\hbar n_s e^*}{m^*} \left(\boldsymbol{\nabla} \varphi - \frac{e^*}{\hbar} \mathbf{A} \right); \tag{1.7}$$

which reduces to the London Eq. 1.2 in the limit of a uniform superconducting phase ($\boldsymbol{\nabla}\varphi \to 0$). Furthermore, the first term in Eq. 1.7 impliles that a non-uniform phase φ results in current flow, and vice versa. This is the incredible consequence of the global phase coherence of the Cooper pairs: variation of the quantum mechanical perameter φ results in the development of a macroscopic current in the condensate.

1.2 The Josephson Junction

Josephson was the first to recognize that if two superconductors are separated by a weak link such as a thin insulating barrier, the phase difference between them would lead to current flow in the junction without a corresponding voltage drop [14]. Such a situation is represented in Fig. 1.1.

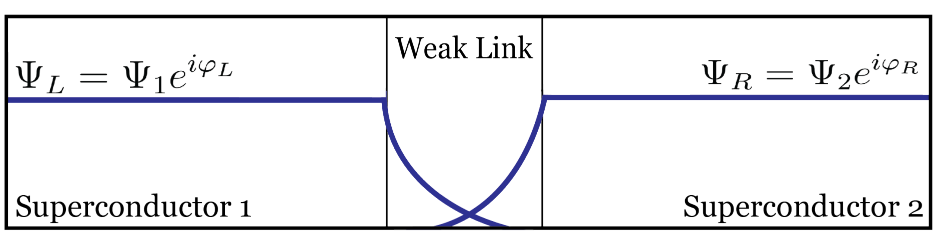

Fig. 1.1: **Diagram of a Josephson Junction (JJ).** The superconductors on the left and right are separated by a weak link, forming the junction. The tails of the Ginzburg-Landau order parameters on each side tunnel into the weak link and overlap.

As indicated in the Figure, the wave functions of the Cooper pairs on each side of the barrier can be written as $\Psi_L = \Psi_1 e^{i\varphi_L}$ and $\Psi_R = \Psi_2 e^{i\varphi_R}$, for the left and right sides respectively, where φ is the phase of the superconducting condensate and $\Psi_{1,2}$ are constants. Since the square of the wave function, $|\Psi^2|$, is equivalent to the electron density n, these can also be written as

$$\Psi_L = n_L^{1/2} e^{i\varphi_L} \quad \text{and} \quad \Psi_R = n_R^{1/2} e^{i\varphi_R}. \tag{1.8}$$

The time-dependent Schrödinger equation can then be applied, giving

$$i\hbar \frac{\partial \Psi_L}{\partial t} = \hbar T \Psi_R \quad \text{and} \quad i\hbar \frac{\partial \Psi_R}{\partial t} = \hbar T \Psi_L, \tag{1.9}$$

where $\hbar T$ is a measure of the transfer interaction through the weak link. Using Eq. 1.8, these can be transformed into

$$\frac{\partial \Psi_L}{\partial t} = \frac{1}{2} n_L^{-1/2} e^{t\varphi_L} \frac{\partial n_L}{\partial t} + i\Psi_L \frac{\partial \varphi_L}{\partial t} = -iT\Psi_R \tag{1.10}$$

and

$$\frac{\partial \Psi_R}{\partial t} = \frac{1}{2} n_R^{-1/2} e^{t\varphi_R} \frac{\partial n_R}{\partial t} + i\Psi_R \frac{\partial \varphi_R}{\partial t} = -iT\Psi_L. \tag{1.11}$$

Multiplying Eq. 1.10 by $n_L^{1/2} e^{-t\varphi_L}$ gives us

$$\frac{1}{2} \frac{\partial n_L}{\partial t} + i n_L \frac{\partial \varphi_L}{\partial t} = -iT (n_L n_R)^{1/2} e^{i(\varphi_R - \varphi_L)}, \tag{1.12}$$

and multiplying Eq. 1.11 by $n_R^{1/2} e^{-\iota\varphi_R}$ gives

$$\frac{1}{2}\frac{\partial n_R}{\partial t} + i n_R \frac{\partial \varphi_R}{\partial t} = -iT(n_L n_R)^{1/2} e^{-i(\varphi_R - \varphi_L)}. \tag{1.13}$$

Equations 1.12 and 1.13 can be separated into four equations by setting their real and imaginary parts equal to each other:

$$\frac{\partial n_L}{\partial t} = 2T(n_L n_R)^{1/2} \sin(\varphi_R - \varphi_L); \quad \frac{\partial n_R}{\partial t} = -2T(n_L n_R)^{1/2}(\sin(\varphi_R - \varphi_L)); \tag{1.14}$$

$$\frac{\partial \varphi_L}{\partial t} = -T\left(\frac{n_R}{n_L}\right)^{1/2} \cos(\varphi_R - \varphi_L); \quad \frac{\partial \varphi_R}{\partial t} = -T\left(\frac{n_L}{n_R}\right)^{1/2} \cos(\varphi_R - \varphi_L). \tag{1.15}$$

For the case where $n_L = n_R$ (i.e. the two superconductors are identical), these can be simplified again, yielding

$$\frac{\partial \varphi_L}{\partial t} = \frac{\partial \varphi_R}{\partial t}. \tag{1.16}$$

Upon examining Eq. 1.14, we can recognize that $-\partial n_L/\partial t = \partial n_R/\partial t$, and that these terms represent a current flow from one side of the junction to the other. Thus, the current flow I through the junction is just

$$I(\varphi) = I_0 \sin\varphi, \tag{1.17}$$

where $\varphi = (\varphi_R - \varphi_L)$ is the phase difference between the two superconductors, and I_0 is a constant proportional to the transfer interaction T. Equation 1.17 is the first Josephson equation.

If a steady voltage V is applied across the junction, Eq. 1.18 instead becomes

$$i\hbar\frac{\partial\Psi_L}{\partial t} = \hbar T\Psi_R - eV\Psi_L \quad \text{and} \quad i\hbar\frac{\partial\Psi_R}{\partial t} = \hbar T\Psi_L + eV\Psi_R. \tag{1.18}$$

Proceeding mathematically the same way as before, we can obtain the second Josephson equation, which predicts that a steady applied voltage V causes a winding of the phase:

$$\frac{d\varphi}{dt} = \frac{2eV}{\hbar}. \tag{1.19}$$

Hence, a fixed DC voltage across the junction produces an *alternating* current with frequency $2eV/\hbar$. This is called the AC Josephson effect.

Andreev later proposed a different microscopic picture of supercurrent flow across a JJ. In Andreev's description, the supercurrent is mediated by the process of Andreev reflection, where an electron colliding with a weak link barrier is retroreflected into a hole with opposite momentum. The hole travels until it collides with the opposing barrier, where it likewise converts back to an electron. This allows for the transfer of Cooper pairs across a junction. Andreev's approach is particularly useful in understanding tunneling in junctions that have relatively transparent barriers or superconducting channels.

In practice, for typical voltages the Josephson frequency is quite high and can be difficult to measure directly. Instead, it is easier to drive the junction with microwave or radio frequency (RF) radiation while also applying a DC voltage. For a combination of AC and DC voltages across the junction of the form

$$V = V_{DC} + V_1 \cos(\omega t), \tag{1.20}$$

the phase difference across the JJ will be given by

$$\varphi = \int \frac{2eV}{\hbar}\mathrm{d}t = \varphi_0 + \frac{2eV_{DC}}{\hbar}t + \frac{2eV_1}{\hbar\omega}\sin(\omega t). \tag{1.21}$$

Substituting into the first Josephson equation, the total current is

$$I = \sum_{-\infty}^{\infty}(-1)^n J_n\left(\frac{2eV_1}{\hbar\omega}\right)\sin\left(\varphi_0 + \frac{2eV_{DC}}{\hbar}t - n\omega t\right), \tag{1.22}$$

where $J_n(x)$ is the n^{th} order Bessel function of the first kind. Examining Eq. 1.22, one can see that if

$$V_{DC} = \frac{n\hbar\omega}{2e}, n = 0, 1, 2..., \tag{1.23}$$

there will be a DC component. Experimentally, the AC Josephson effect manifests as plateaus in the junction's current-voltage profile which occur at voltages that are integer multiples of $\hbar\omega/(2e)$. These plateaus are called *Shapiro steps* [15]. Because Eq. 1.23 relates frequency to voltage in terms of only fundamental constants, this effect has been of great importance to metrologists and is the basis for the voltage standard [16].

Typical superconductor-insulator-superconductor JJs have barriers that are not relatively transparent, and this yields CPRs which follow the simple sinusoidal form of Eq. 1.17. In some types of JJs, however, the junction may possess a CPR that is non-sinusoidal. One possible result of this deviation is the appearance of subharmonic structure in Shapiro measurements, so that the voltage plateaus (steps) manifest at fractional values of the expected voltages $n\hbar\omega/(2e)$. That is, in addition to integer values, n may be 1/2, 1/3, etc. In single junctions, these fractional steps may only appear systematically if the CPR is not a pure sinusoid [17].

Thus far we have considered φ to be constant spatially over the cross-sectional area of the junction, but this is generally not the case in large junctions or in the presence of a magnetic field. Indeed, in the presence of gauge field $\mathbf{A}$, we must replace φ with the *gauge invarient phase difference*

$$\phi = \varphi_L - \varphi_R - \frac{2e}{\hbar}\int_L^R \mathbf{A}\cdot d\mathbf{l}, \tag{1.24}$$

where φ_L and φ_R are the phases of the two superconductors and the integral is taken from the left superconductor, through the barrier, to the right superconductor. This has major consequences for the case of a wide (i.e. not point-like) junction (see Fig. 1.2).

Since the order parameter must be single-valued to be physically meaningful, the total change in ϕ as we pass around the closed loop must equal $2\pi n$. Upon enforcing this condition and adding up the phase around the loop shown in Fig. 1.2, one can find that

$$\phi(x) - \phi(x+dx) = \frac{2\pi\Phi}{\Phi_0}, \tag{1.25}$$

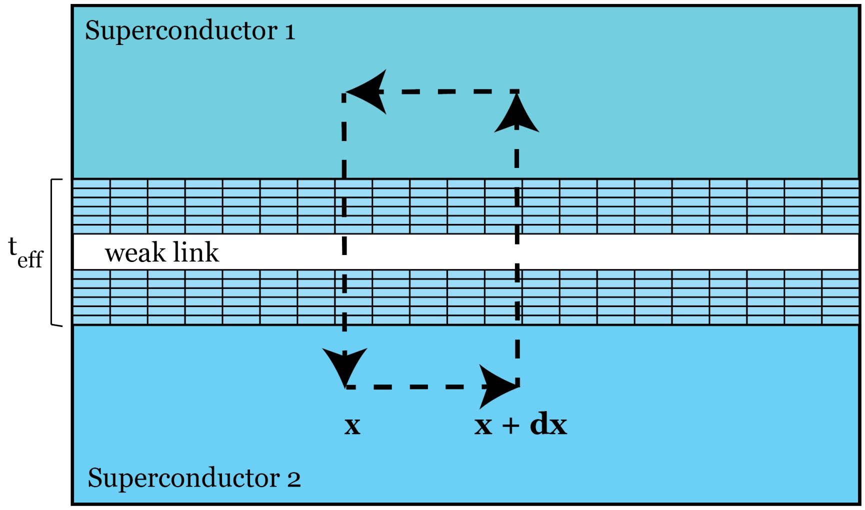

Fig. 1.2: **Schematic of a wide JJ** with effective barrier thickness $t_{eff} = t + 2\lambda_L$. B_z is directed out of the page, and dx is taken to be very small.

where $\Phi = B_z t_{eff} dx$ is the total magnetic flux enclosed in the loop, t is the barrier thickness, $t_{eff} = 2\lambda_L + t$ is the effective barrier thickness, and $\Phi_0 = h/(2e)$ is the superconducting flux quantum. Rearranging this, we can obtain

$$\frac{d\phi}{dx} = \frac{2\pi}{\Phi_0} B_z t_{eff}. \tag{1.26}$$

Integrating Eq. 1.26 and using Eq. 1.17 reveals that the supercurrent density in the extended junction is given by

$$J = J_c(z, x) \sin\left(\frac{2\pi}{\Phi_0} t_{eff} B_z x + \phi_0\right), \tag{1.27}$$

where ϕ_0 is an integration constant. Hence, a uniform magnetic field B_z produces a *spatial* variation in ϕ, which then results in a sinusoidal variation of the current density along the length of the junction.

Of course, the macroscopic observable in a typical electrical measurement is not the current density J but rather the total current through the junction. Under the assumption that the critical current density $J_c(z,x)$ is uniform, one can find the maximum Josephson supercurrent in the device to be

$$I(\Phi) = I_c \left| \frac{\sin \frac{\pi\Phi}{\Phi_0}}{\frac{\pi\Phi}{\Phi_0}} \right|. \tag{1.28}$$

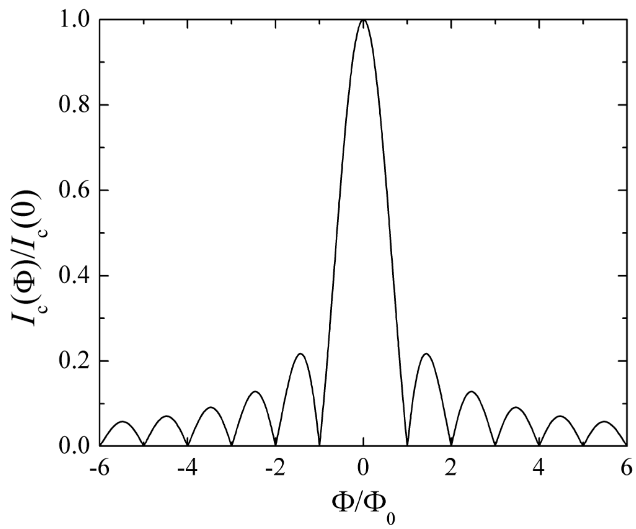

Fig. 1.3: **A standard Fraunhofer-like magnetic diffraction pattern of a uniform Josephson junction**; Figure from Ref. [18].

Plotting 1.28 results in a *fraunhofer*-like diffraction pattern, shown in Fig. 1.3. This is analogous to the single-slit diffraction pattern in optics, where interference results from the wavelike character of light. In the junction, it is the phase of the macroscopic order parameter that causes quantum interference [19]. Observation of this magnetic diffraction pattern was a key experimental confirmation of the Josephson effect.

1.3 The Tilted Washboard Potential

In this section, which loosely follows Chapter 6.3 of Ref. [10], I will discuss how I modeled the dynamics of Josephson junction behavior. This is most commonly accomplished using the resistively and capacatively shunted junction model (RCSJ), with the equivalent circuit depicted in Fig. 1.4. Here, C is the total capacitance from the junction electrodes, while R represents the ohmic resistance which may be due to an actual resistor connected across the junction, or to loss from quasiparticles tunneling across the junction, or to other dissipation processes. For simplicity I will assume R is frequency and voltage independent, although many situations can arise where this is not the case.

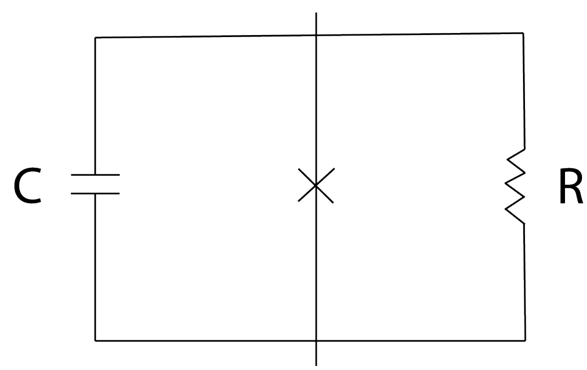

Fig. 1.4: **The RCSJ circuit model**, which includes an ideal JJ shunted by resistance R and capacitance C.

When the junction is current-biased, the total current passing through the three parallel elements of the circuit can be written as

$$I = C\frac{\partial V}{\partial t} + \frac{V}{R} + I_c \sin(\phi). \tag{1.29}$$

Using Eq. 1.19, and introducing the time scale $\tau = (2eI_c/\hbar C)^{1/2}t = \omega_p t$, this can be rewritten in terms of the phase to obtain an inhomogeneous nonlinear second order differential equation

$$\frac{I}{I_c} = \frac{d^2\phi}{d\tau^2} + \frac{1}{Q}\frac{d\phi}{d\tau} + \sin(\phi). \tag{1.30}$$

Here, $\omega_p = (2eI_c/\hbar C)^{1/2}$ is the Josephson plasma frequency, and $Q = \omega_p RC$ is the quality factor of the junction.

Fortunately, Eq. 1.30 has a helpful mechanical analog. Indeed, Eq. 1.30 is just the equation of motion of a particle with mass $m = (\hbar/2e)^2 C$ moving in the ϕ-direction along a "washboard"-like potential

$$U(\phi) = -\frac{\hbar}{2e} I_c \cos(\phi) - \frac{\hbar I}{2e}\phi \tag{1.31}$$

while being subjected to linear damping. The potential $U(\phi)$ is plotted in Fig. 1.5. You can picture the phase particle as moving along the washboard surface under the influence of gravity, with its movement being opposed by a "drag force" given by

$$\left(\frac{1}{R}\right)\left(\frac{\hbar}{2e}\right)^2 \frac{d\phi}{dt}. \tag{1.32}$$

The bias current I modifies the angle of the washboard's tilt.

1.4 Topological Insulators and Topological Crystalline Insulators

Topological materials form the final critical part of my experimental research.

Topology is the branch of mathematics that deals with objects or spaces that may be transformed into one another via continuous deformation – that is, to pre-

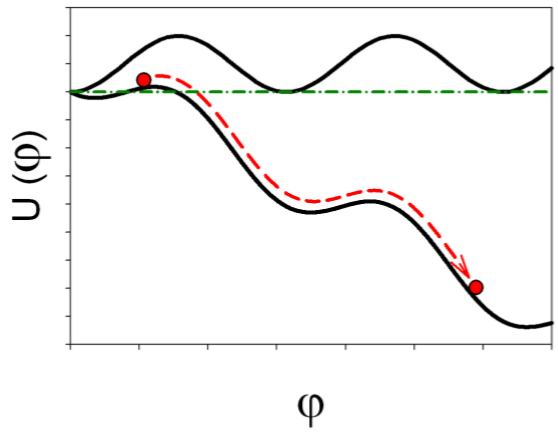

Fig. 1.5: **Tilted washboard potential for the RCSJ model** with zero current bias (upper curve) and nonzero bias (lower curve); Figure from Ref. [20].

serve the topological class of an object, it may be stretched and squeezed like rubber but it cannot be cut or broken. The classic example for a shared topological invariant is "donut = coffee cup"; meaning that it is possible to smoothly transform a torus-shaped surface into a coffee cup-shaped surface, since both have one hole. To make the bridge to topology's application in condensed matter physics, consider the example of a loop and a trefoil knot (see Fig. 1.6). It is not possible to convert the trefoil knot into the loop without cutting the string; therefore, their topological invariants are not the same.

Similarly, a topological insulator (TI) is a material that does not share an invariant with a conventional insulator (e.g. the vacuum is a conventional insulator). This means that joining a TI to a conventional insulator necessitates a transformation at their interface. The interface between two materials is analogous to making a cut in a trefoil knot so that the rope ends can be joined into a simple loop. The result is the appearance of surface states at the interface which are topologically protected, i.e. insensitive to scattering and disorder. Thus, a TI acts as an insulator

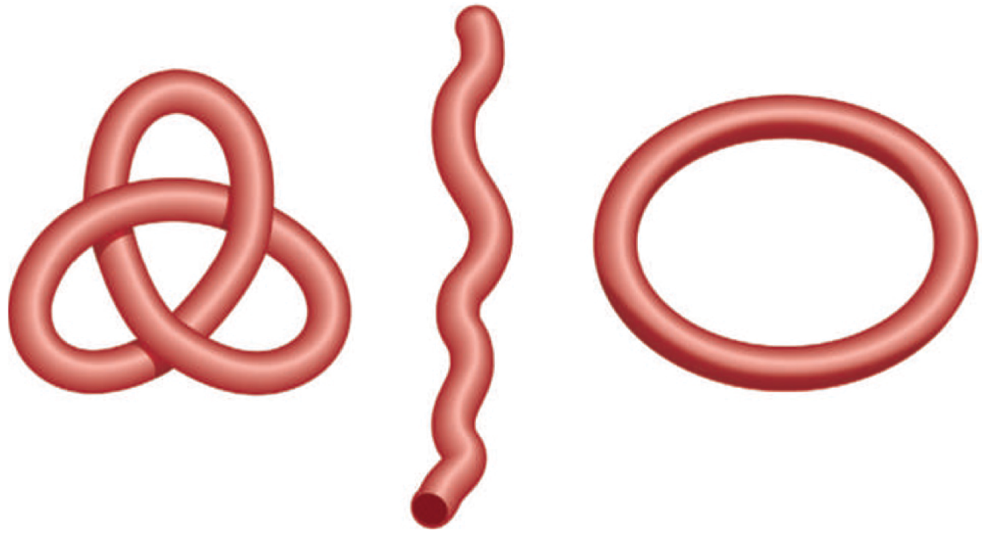

Fig. 1.6: **The trefoil knot and the simple loop** are topologically nonequivalent. This helpful figure is from Ref. [21].

in the bulk but has a metallic surface.

In general, TI surface states are protected by time-reversal symmetry. It is also possible for a topological material to instead have surface states that are protected by crystal, or mirror, symmetry; and these are called topological crystalline insulators (TCI)s. In this dissertation, I will describe my experimental results on both types of topological insulators.

When a TI comes into contact with a superconductor, the proximity effect causes superconductivity to leak into the TI, forming a "topological superconductor" which is expected to be capable of hosting Majorana fermions, particles that are their own antiparticles. Fundamental interest in these new particles, the prospect of applying them in topological quantum computing, and unusual properties of these particles (Majoranas follow non-Abelian statistics) have driven much relevent work in this field.

Chapter 2: Device Fabrication and Measurement

2.1 *Electron Beam Lithography and Metal Deposition*

In this Chapter, I will give a detailed walkthrough of the experimental processes I used to make and measure the devices I studied in this thesis. All of the devices were fabricated using electron beam lithography (EBL); a schematic of the lithography process is shown in Fig. 2.1. First, I prepared the substrates: for PbSnTe devices, I used GaAs, and for SnTe nanowires the substrate was Si/SiO_2. In both cases I received these chips with the TI already grown on top of them by exceptional collaborators. In order to control the exact locations of the devices I wanted to write–for example, so that my JJs landed precisely on top of the randomly dispersed nanowires–I first created some 10 $\mu\times$ 10 μm gold squares to use as alignment marks. The marks, which I patterned in a grid with each mark 200 μm away from its adjacent neighbors, can be seen in Fig. 2.2(a).

To make these marks, I cleaned my samples in a beaker of acetone for 5 minutes, then cleaned them in isopropyl alcohol (IPA) for 5 minutes. I blow dried the surfaces with high purity nitrogen, and then I set the samples onto a hot plate for 5 minutes at 185°C. With the substrates clean, I spin-coated a layer of 950k A4 poly(methyl methacrylate) (PMMA) for a resist. I set the spin coater for 5000 rpm

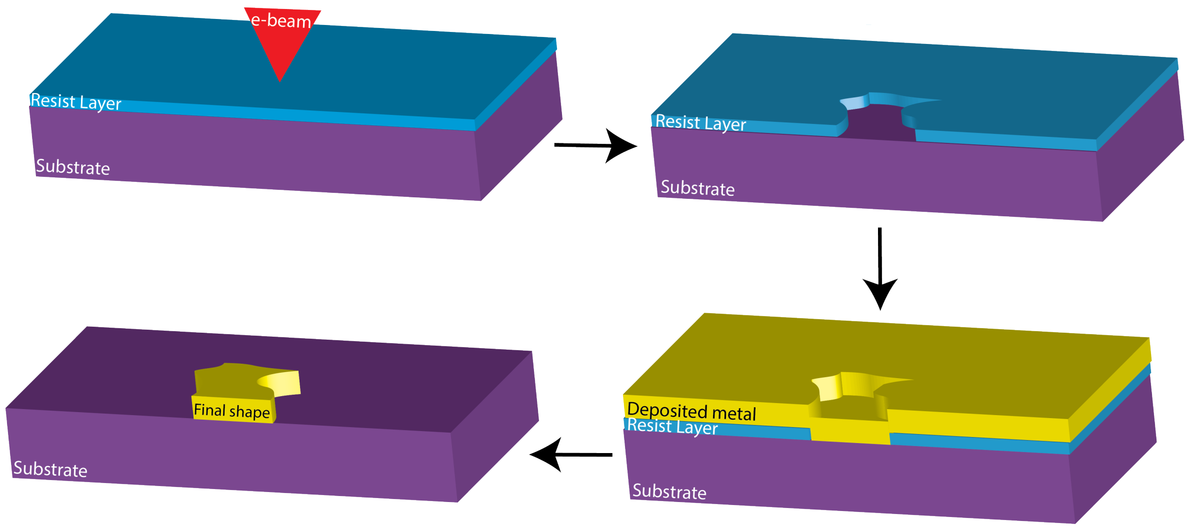

Fig. 2.1: **The device fabrication process:** e-beam exposure to the spun sample, followed by development, metal deposition, and liftoff.

for one minute, and when it was done, I gave the resist layer a quick eyeball check to ensure that the coating looked even. When I was satisfied with the spin, I returned the samples to the 185°C hotplate and baked them for 15 more minutes. At this point, the chips were ready to be loaded into the Elionix ELS-G100 100 kV Electron Beam Lithography System. My standard dose for lithography was 1050 μC/cm^2. To make alignment marks, I used a beam current of 100 nA.

Once my samples were inside the Elionix, I selected the alignment mark pattern I had at the ready, which I had previously designed using the AUTOCAD computer-aided design software. The CAD file told the electron beam where to trace. Exposure to the beam broke the PMMA polymer into smaller chains of molecules that could be dissolved by a solvent, which in my case was a 1:3 mixture of methyl isobutyl ketone and IPA. When the samples had been removed from the Elionix, I poured the solvent into a beaker, then picked up each one with my tweezers and swirled it around in the mixture for one minute. Once the minute passed, I squirted off the surface of the chips with IPA from a squirt bottle, and then dried them with high purity nitrogen.

The next step was metal deposition using an AJA electron beam evaporator. In an evaporator, electrons are accelerated toward a tungsten crucible containing the desired material, which is consequently heated, causing the material to evaporate onto a waiting substrate. For the alignment marks, I performed an *in situ* Ar etch at 50 W for one minute after loading the samples into the chamber. Then, I deposited 4 nm of Ti followed by $\sim$70 nm of Au. The Ti acted as a sticking layer between the Au and the substrates.

Once I removed the samples from the evaporator, it was time for lift off. I placed them into a covered beaker of n-methyl pyrrolidone (Remover PG) and left them for 3 or more hours on a hot plate set to 60°C. When the time passed, the metal layer looked crinkly and was ready to be removed by a few seconds of sonication. If the samples were sensitive, however–for example, if they were nanowire samples where sonication might cause the wires to fly off the chip–I instead squirted the surface of the chips with acetone and IPA until the unwanted metal was removed. When satisfied, I rinsed the samples again with acetone and IPA, and dried them with nitrogen.

At this point, the alignment marks were finished, and I could repeat the lithography process, this time patterning the actual devices using the marks as a positioning guide. My junctions were made with either 70 nm or 200 nm of deposited Al. For the thinner 70 nm devices (akin to the JJs in Chapter 3), the spinning process

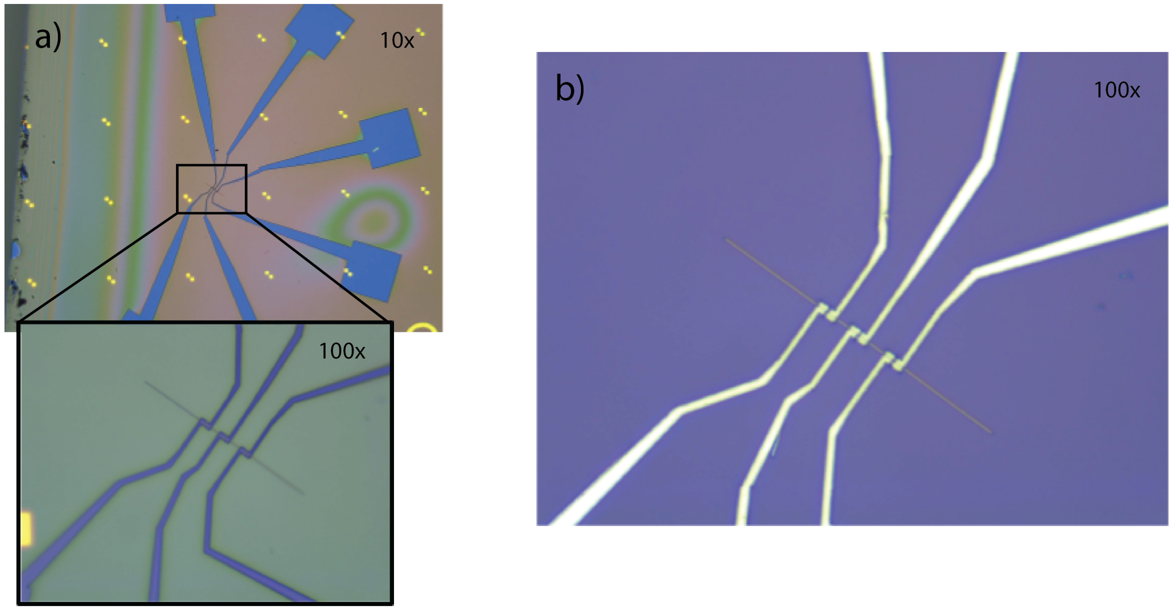

Fig. 2.2: **Optical micrographs of patterned junctions.** (a) Images of a series of JJs that I patterned atop a SnTe nanowire, taken using an optical microscope immediately after the development step. The pattern is shown at both 10x and 100x magnification. The gold alignment marks have dimensions of 10 μm $\times$ 10 μm. (b) The same pattern after the metal deposition and liftoff steps, at 100x magnification.

was exactly the same as that described above. For the thicker 200 nm devices (akin to the JJs in Chapter 4), it was necessary to add a second layer of PMMA after the first was finished–this time, I spun 950k A4 PMMA at 5000 rpm for one minute. I then baked the samples for an additional 15-20 minutes on the 185°C hotplate.

I used a dose of 1050 μC/cm^2 for the device patterning. Since the devices had much finer features than the alignment marks, it was necessary to reduce the beam current for these writes to allow for greater precision. The junctions themselves, as well as the nearby leads (that is, any part of the pattern in an area of a few microns surrounding the JJs) were written with the fine 100 pA beam. The leads towards the outsides of the patterns, which did not require as much precision, could be written at 1 or 5 nA to speed up the process.

I developed the samples the same way as described above, and then loaded them into an AJA International sputtering system. Similarly to before, I first performed an *in situ* Ar etch at 50 W for one minute, and then I sputtered a sticking layer of ~4 nm of Ti. I used aluminum as my superconductor. Before depositing it, I brought the substrate heater to 200°C, since I found that heating during this time greatly improved the electrical contact between the Al and the TI in my final devices. I sputtered either 70 nm or 200 nm of Al according to my needs. Lift off was performed exactly the way I described for the alignment marks.

Working Josephson junctions that I created had a spacing between the superconducting leads of around 80 nm. For this reason, the lithography process needed to be very precise; else the leads of the JJ ended up either too far apart, or shorted together.

Figure 2.2 displays example optical images of a developed pattern in PMMA, followed by the device that resulted.

2.2 Measurement Techniques

To measure a completed junction, I stuck the sample (usually about 4 mm × 4 mm in size) onto a small carrier using dried PMMA to hold it in place. I used an ultrasonic wire-bonder with aluminum thread to create electrical connections between the carrier and the leads of the patterned devices. Then, I used vaccuum grease to stick the small carrier into a larger carrier designed to connect to the dilution refrigerator, and bonded from the small carrier to the large carrier. I did this because I wanted the bonds that connected to the actual device to remain undisturbed, even if I ended up needing a second measurement of the sample. An image of a sample bonded to the carriers is shown in Fig. 2.3(a).

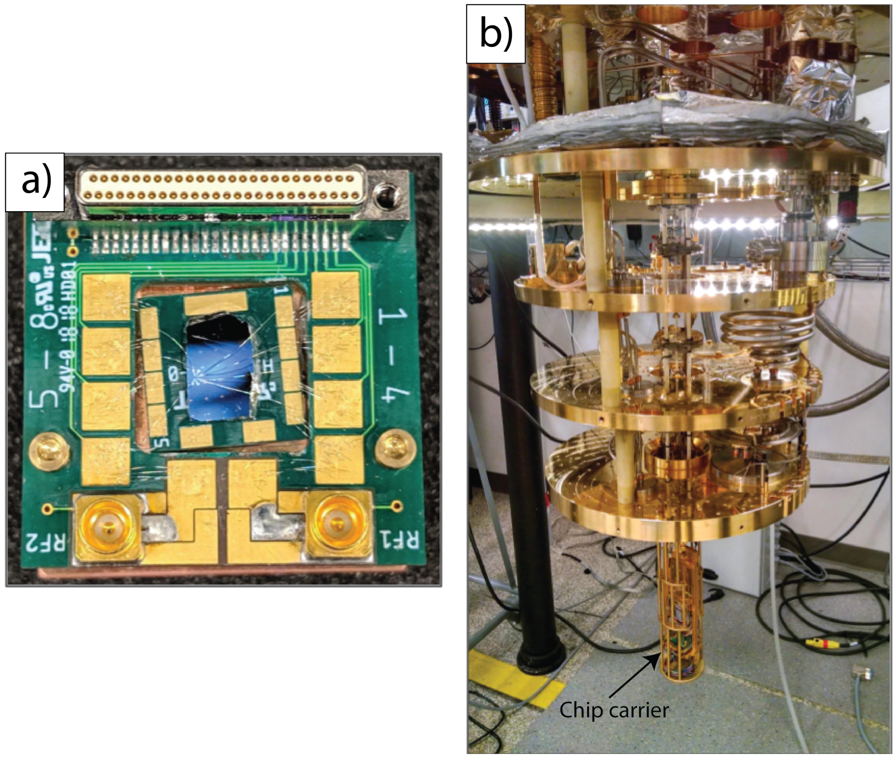

Fig. 2.3: **Loading devices into a dilution refrigerator.** (a) Wire-bonded devices on a chip carrier. (b) One of the lab's dilution refrigerators with the outer vacuum cylinders removed, showing the position of the loaded carrier.

With the devices connected, I loaded them into a dilution refrigerator as shown in Fig. 2.3(b). The refrigerator exploited the properties of the superfluid and normal fluid phases of ^{3}He and ^{4}He mixtures to cause the system to cool. This process allowed us to reach base temperatures of around 50 mK. Once cold, I applied a current bias and/or RF radiation to the superconducting devices, and I measured their differential resistance under various conditions using a standard lock-in amplifier technique.

Chapter 3: A Skewed Current-Phase Relation in Josephson Junctions with Weak Links of PbSnTe

3.1 Introduction

Here I report on the fabrication and measurement of Josephson junctions that were made using both $Pb_{1-x}Sn_xTe$ (topologically nontrivial) and PbTe (topological trivial) as weak link materials between the two aluminum leads. The contents of this chapter have been published in *Physical Review Letters* [22]. I characterized these junctions by measuring DC $I-V$ curves, the $I_C R_N$ product and its temperature dependence, the magnetic diffraction pattern, and the AC Josephson effect. The most striking deviation I found between the topologically-trivial and nontrivial junctions occured under microwave radiation: in addition to finding Shapiro steps observed at DC voltage values consistent with $nhf/2e$, the TCI JJs also exhibited steps at fractional values, consistent with a strongly nonsinusoidal current-phase relation (CPR). As I discuss below, I confirmed through numerical simulations of the AC Josephson effect in a resistively-shunted junction model that such subharmonics can be produced if the CPR is not sinusoidal. The subharmonic structure I report here was only found in weak-link materials with low mobility, and I discuss the origin of this phenomena in terms of helical states predicted to exist in this a TCI.

3.2 Methods

$Pb_{0.5}Sn_{0.5}Te$ and PbTe weak-link Josephson junctions with a width of $1\,\mu$m and length between 50 and 120 nm were patterned using electron-beam lithography (see the inset of Fig. 3.1). The deposition of the electrodes defining the junctions began with an in-situ Ar rf plasma etch for 60 s at 50 W, followed by sputtering of Ti/Al (3 nm/ 70 nm). During the deposition of the aluminum, the substrate was heated to 100^{o}C. The $Pb_{0.5}Sn_{0.5}Te$ or PbTe films were then removed through a reactive ion etch of Ar/H2 (20:2) over the entire surface, except underneath the Al, in between the Al leads (the Josephson junction), and in a 2μm region on the left and right side of the Al, which were protected by a PMMA mask. An SEM image of a completed device is shown in the inset of Fig. 3.1. Completed devices were then cooled to 50 mK and I measured the differential resistances $R = dV/dI$ as a function of current I (I_{bias} between 1-10 nA) with a lock-in amplifier. A total of 14 junctions showing superconducting properties were measured, two of which were in detail demonstrated in this chapter (see the supplementary information for Ref. [22] for additional data). Tunneling spectroscopy was obtained by sweeping a DC current source, resulting in the plots of R vs. $I_{\rm DC}$ at different temperatures T (see Fig. 3.1. The current at which $R(I_{\rm DC})$ changes from zero to the peak values determined the switching current of the junction, which I assumed to be a reasonable measure of the critical current. The $I_C R_N$ product (R_N is the normal state resistance of the junction) rises from zero at T=500 mK to $\sim$ 10 μV at base temperature (see Fig. 3.1).

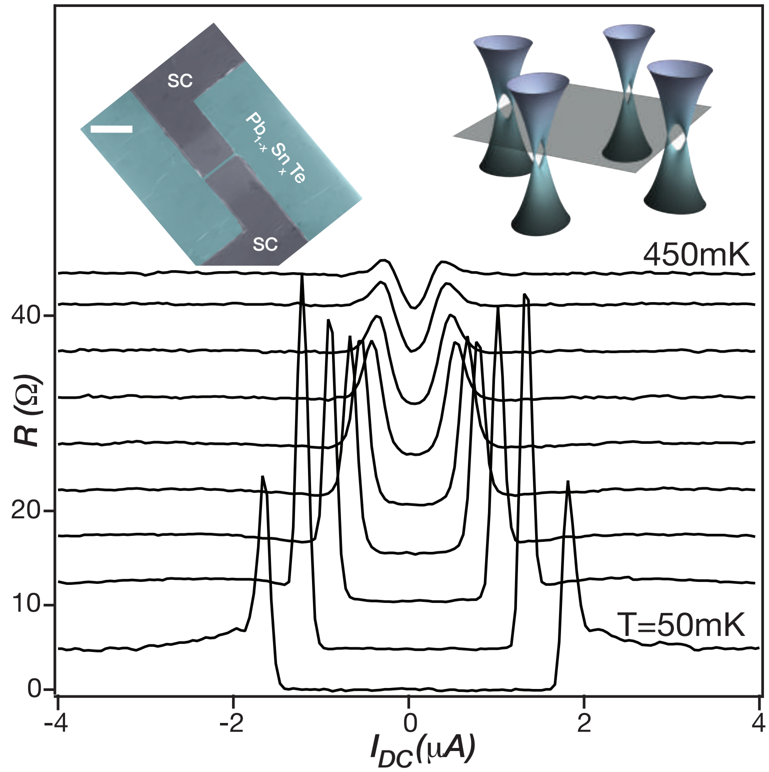

Fig. 3.1: **Device 1: Temperature dependence of the differential resistance $\boldsymbol{R}$ versus current $\boldsymbol{I}$**, where superconducting features appear below T=500 mK. The peaks in R occur at values $I_{\mathrm{DC}} = I_{\mathrm{C}}$. (Inset, upper left) shows a scanning electron micrograph of a device similar to the ones studied in this chapter, showing two superconducting (SC) aluminum leads (dark grey) and the TCI material $\mathrm{Pb}_{1-x}\mathrm{Sn}_x\mathrm{Te}$ (green). The scale bar shown in white is 1 μm. The spacing between the two SC leads is 100 nm. (Inset, upper right) Schematic of the band structure of $\mathrm{Pb}_{1-x}\mathrm{Sn}_x\mathrm{Te}$ where 4 Dirac cones appear across the $\overline{X}$ point in k-space [23].

3.3 Results and Discussion

3.3.1 The magnetic diffraction pattern

Application of a perpendicular magnetic field B normal to the substrate surface of Device 1 allowed for a variation of the superconducting phase difference across

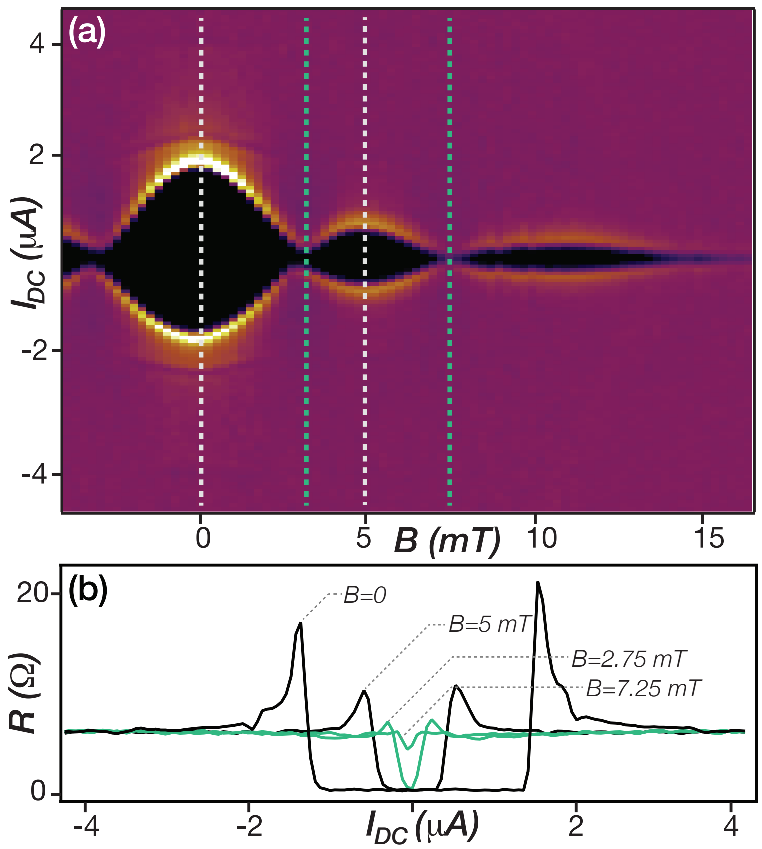

Fig. 3.2: **The magnetic diffraction pattern for Device 1.** (a) Plot of $R(B, I_{\mathrm{DC}})$, revealing a Fraunhofer-like pattern consistent with a (nearly) uniform supercurrent across the width of the device. (b) One-dimensional cuts in the data from (a) at B=0, 5.00 mT (black) and 2.75, 7.25 mT (green), where the latter two show the variation in R between at the first and second minimum in I_{C}.

the width of the junction. A plot of R as a function of I_{DC} and perpendicular magnetic field is shown in Fig. 3.2(a). In conventional junctions with a sinusoidal CPR and a uniform critical current density across the device, a Fraunhofer pattern in the magnetic-field dependence of R is expected [24]. A good Fraunhofer pattern was useful for eliminating the possibility that the supercurrent in Fig. 3.1 was from an electrical short between the superconducting leads. The observed pattern was consistent (at least approximately) with the current density being uniform over the width of the device. In particular, Fig. 3.2(a) shows a pattern that is reminiscent of a Fraunhofer pattern except for two important deviations: the width of the central lobe is not twice the width of the other two, and while $I_{\mathrm{C}} \to 0$ at the second minimum (B=7.25 mT), it remains finite at the first minimum (B=2.75 mT). For more clarity, cuts of R at B=0, 2.75, 5.00, and 7.25 mT are shown in Fig. 3.2(b). The observed deviation of the magnetic-field dependence from a Fraunhofer pattern is consistent with observations of other 3D topological insulators [25, 26], and has been used in the past to argue for the presence of nonsinusoidal current-phase relations [27]. However, a simple modification to allow for the critical current density to smoothly vary along the width of the device can also produce a similar modification of the Fraunhofer pattern. Hence, measurements of this type cannot extract a unique CPR. Also visible in Fig. 3.2(b) is a small amount ($\sim$10%) of hysteresis as a function of I_{DC}. Since we the Stewart-McCumber parameter to be small in junctions with this geometry [28], we ascribe this hysteresis to self heating of the electrons [29].

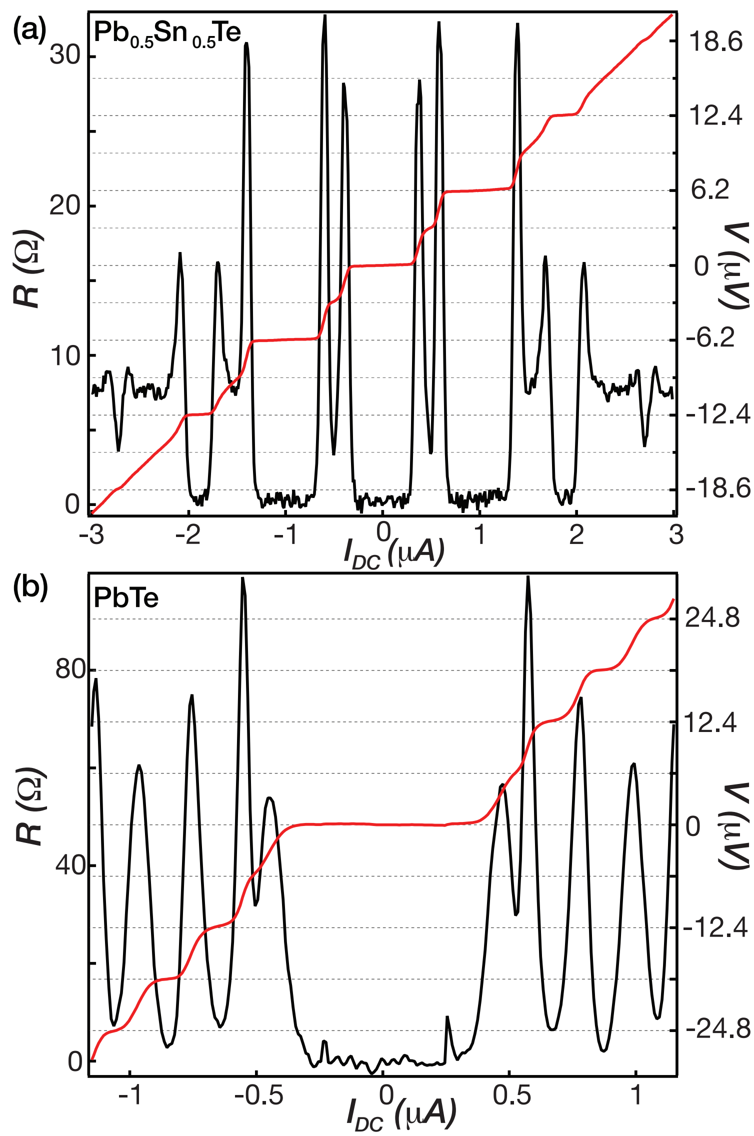

Fig. 3.3: **Device 1: comparison of $Pb_{0.5}Sn_{0.5}Te$ and PbTe characteristics at f=3 GHz and applied RF power of -6.75 dBm.** (a) Plot of R vs I showing minima at expected values for Shapiro steps and at half integer values. Numerically integrated $I - V$ data (red) shows Shapiro steps at $nhf/2e$=n∗6.2μV and additional features at fractional values of $\frac{1}{2}$ and $\frac{3}{2}$. (b) By comparison, a PbTe device showing only integer values of the Shapiro steps, both in R (black) and $I - V$ (red).

For a sinusoidal current-phase relation, a microwave voltage at frequency f applied to the junction produces steps in the $I - V$ curves at voltages $nhf/2e$ [30]. These steps will appear as minima in the differential resistances R. Fig. 3.3(a) (black curve) shows R vs I_{DC} for an applied microwave frequency of 3 GHz. Well-defined minima of R can be observed at values of $nhf/2e$. In Fig. 3.3 I also show $I-V$ curves generated from a numeric integration of the differential resistance. The steps in I associated with the minima in R are clearly seen in th $I-V$ curves (Fig. 3.3(a), red). The deepest minima in R, corresponding to steps at intervals of $hf/2e$=6.2 μV, are in agreement with expectations. Besides these pronounced minima, there is additional structure. Structure between the conventional minima can be caused by higher harmonics in the CPR, including fractional values of the AC Josephson effect. The integrated $I-V$ shows small subharmonic features at $hf/4e$ and $3hf/2e$, demonstrating that these junctions may not have a conventional $\sin(\varphi)$ CPR.

To investigate whether the half integer steps arise from a non-topological property of the weak link, I also fabricated junctions from the topologically trivial material PbTe. Figure 3.3(b) shows my measurements of R vs I under 3 GHz radiation. I observed a conventional Shapiro step behavior with no obvious dips in between the integer minima. The $I-V$ curve (red) shows only plateaus at multiples of 6.2 μV, which is consistent with the current-phase relation arising primarily from a single $\sin(\phi)$ term. Measurements of this PbTe junction at higher powers and frequencies also showed only integer Shapiro steps.

Further information on the CPR of the $Pb_{0.5}Sn_{0.5}Te$ device is revealed by plotting the power dependence of the subharmonic structure. Figure 3.4(a) shows a plot of R for conventional applied RF powers P between -27.25 and -9 dBm, for f=2.2 GHz. Conventional Shapiro steps are seen at integer multiples of $hf/2e$

(labeled by number in white) and follow a Bessel function power dependence, as expected [30]. In addition, different subharmonic structure is observed between different primary plateaus (indicated by white arrows). For example, at certain values of P, a single dip is observed between steps 0 and 1, while at the same power two dips are seen between steps 3 and 4. This secondary structure follows a more complicated pattern: as a function of power and I_{DC}, one or sometimes two minima were seen.

A line cut showing R vs I_{DC} (see Fig. 3.4(b)) taken at P=-15 dBm (grey line) shows the intricate behavior observed in R. If only the fundamental and a second harmonic existed in the CPR so that $I_S \propto \sin(\varphi)+\sin(2\varphi)$, only a single dip in R would be present between conventional Shapiro steps. This is not the case, and this suggests even higher order terms may be present.

3.3.3 Theory and simulations

My AC Josephson effect data suggests that multiple harmonics are present in the CPR of the $Pb_{0.5}Sn_{0.5}Te$ junctions. Deviations from a sinusoidal CPR in low-capacitance weak link junctions are expected when the weak link has channels of high transparency [31]. Recently, such deviations of the CPR have been seen in junctions made from one-dimensional nanowires with strong spin-orbit coupling [32], graphene [33], and the three-dimensional topological insulator HgTe [34]. Common to these three are the high values of the electronic mobility, and each experimental report cited highly-transmitting electronic channels as the underlying cause of the skewed CPR. This feature serves in stark contrast to the measured Hall mobility in the devices under study in this paper; for example, our observed mobility is $\sim$250 times less than the reported mobility of the 3D TI HgTe [34].

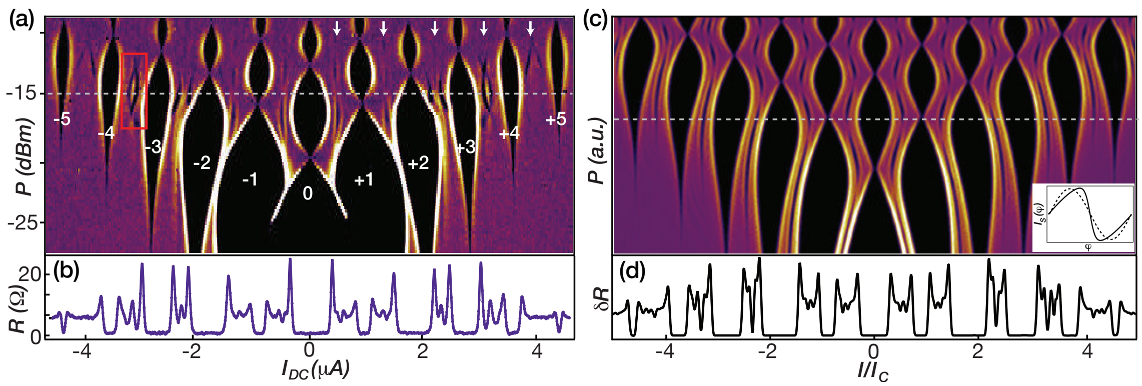

Fig. 3.4: **Power dependence of the AC Josephson effect in $Pb_{0.5}Sn_{0.5}Te$ junctions.** (a) Shapiro map taken at f=2.2 GHz. In addition to the main Shapiro steps (black regions indicated by white numbers), structure in between the primary steps is seen (indicated by white arrows). (b) A line cut of R vs I_{DC} taken along the grey line in (a). (c) Simulation of the RSJ model using a CPR for KO-2 theory for a ballistic Josephson junction, simulated over a similar range of parameters as the data in (a). The saw-tooth behavior of the CPR is necessary to mimic the data. (Inset) A plot of the CPR for the KO-2 theory (solid line) is compared to a pure sine wave (dashed line). (d) A line cut of the simulated differential resistance δR vs I_{DC} qualitatively reproduces that observed in the experiment.

To confirm that a current-phase relation possessing higher harmonics can yield results that are similar to the data shown in Fig. 3.4(a), I performed a numerical integration of the resistively shunted junction (RSJ) model [30] (see the supplementary info for Ref. [22] for details of the simulations). The simulations were done for the CPR as a function of transparency of the weak link, where higher transparency results in a more skewed CPR [29, 31]. For example, Fig. 3.4(c) shows results from the simulation of the RSJ model using a current-phase relation with unity transparency:

$$I_S(\varphi) = \frac{\pi\Delta}{eR_N}\sin(\varphi/2)\left(\tanh\frac{\Delta\cos(\varphi/2)}{2k_BT}\right). \tag{3.1}$$

This CPR is shown in the inset of Fig. 3.4(c), plotted using an estimated value for Δ of k_B*500 mK. This temperature corresponds to that at which the $I_{\mathrm{C}}R_{\mathrm{N}}$ product deviates from zero.

While not all the features I see in the data are captured by the simulation, a side-by-side comparison of the line cuts of the experimental data and the simulation (Fig. 3.4(d), from cut taken along the grey line of Fig. 3.4(c)) shows qualitative agreement, reproducing the key features of the subharmonic structure. The most important distinguishing features of this CPR are the appearance of peaks centered between successive integer Shapiro steps and the unequal values of consecutive dips seen in the one-dimensional cut of the simulation (Fig. 3.4(d)). I only found these features in simulations that had a strongly-skewed current-phase relation resulting from the existence of higher harmonics in $I_S(\varphi)$ [35]. However, I was not able to account for all of the observed behavior despite a rather comprehensive search through different types of possible current-phase relations (e.g. a CPR for diffusive systems) [35]. A feature that conventional or skewed CPRs fail to capture is fine structure in the power dependence of the subharmonic structure (see, for example, the region highlighted by the red box in Fig. 3.4(a)). Whereas our data shows subharmonic lines crossing, simulations with conventional CPRs that I examined always yielded lines that never crossed.

Given the low Hall mobility of our samples, what might be the origin of electronic modes with high transmission? Recent experimental work by Sessi et al. investigating the surface of the TCI (Pb,Sn)Se has revealed one-dimensional, topological spin-filtered channels existing on step edges that break translational symmetry (called odd step edges) [36]. These 1D states only exist when the material is doped in the topological regime and they argue that this is a phenomena general to TCIs, not just the material under study. Such 1D modes have been been reported in another TCI material, Bi2TeI [37], and in a weak topological insulator $Bi_14Rh_3I_9$ [38] – of which TCIs are a subclass. These observations are consistent with these high transmission channels being a general feature of TCIs. In particular, the existence of such step-edge conducting channels would account for the skewed CPR and the measured differences between $Pb_{1-x}Sn_xTe$ and PbTe. The density of odd step edges in our samples can be estimated from the crystallographic offset of the GaAs wafer used to grow the $Pb_{1-x}Sn_xTe$, resulting in ∼5 per 100 nm. This number represents the minimum number, since steps edges can also be produced during growth. Each 1D mode is expected to contribute $\frac{e\Delta_0}{\hbar} \approx 10\,\mathrm{nA}$ [39], so at least 500 nA of the critical current could come from these modes. If not all the critical current comes from 1D modes, the rest will likely come from the bulk, which I expect may have a more conventional CPR. To check whether the subharmonic features survive an additional bulk supercurrent, I simulated a combination of a conventional sinusoidal CPR and the CPR from Eq. 3.1, and the subharmonic features survive.

3.4 Conclusion

In this chapter I described the fabrication and measurement of JJs with weak links made from the topological crystalline insulator $Pb_{1-x}Sn_xTe$. I described the properties of these junctions, and compared them to JJs fabricated with weak links of PbTe, a similar material that is topologically trivial. The most striking differences were be seen in measurements of the AC Josephson effect: JJs made with $Pb_{1-x}Sn_xTe$ exhibited a rich subharmonic structure, consistent with a skewed CPR. This structure was absent in JJs fabricated from PbTe. I discussed the possible origin of this effect and how this novel behavior may be arising from a topologically nontrivial surface state.

Chapter 4: Josephson Detection of Time Reversal Symmetry Breaking Superconductivity in SnTe Nanowires

4.1 Introduction

For conventional JJs, the sinusoidal current-phase relation $I_S(\phi) = I_C \sin(\phi)$ necessitates a statement of time reversal symmetry, which is reflected in the anti-symmetric property $I_S(\phi) = -I_S(-\phi)$ of the CPR [31]. However, the CPR needs not be a sinusoid, as I discussed in Chapter 3. An example is the case of JJs were made with with weak links made of $Pb_{0.5}Sn_{0.5}Te$. In these JJs, higher order processes arising from multiple Andreev reflections can add higher harmonics to the CPR. Nevertheless, time-reversal symmetry in these junctions still holds.

JJs have also been created with superconductors or weak links which possess broken time reversal symmetry (BTRS). These include JJs made with ferromagnetic weak links [40, 41] or with spin-orbit coupled materials in the presence of a magnetic field [42]. Other possible BTRS materials include those that maintain time-reversal symmetry in the normal state but break this symmetry upon entering the superconducting state, including multicomponent superconducting states in multiband materials [43, 44], grain boundaries in d-wave superconductors [45, 46] and in topological p-wave superconductors, including possibly Sr_2RuO_4, although the nature of superconductivity in this material is still disputed [47]. Junctions comprised of these materials exhibit common characteristics that arise from BTRS. First, the measured critical current that depends on the sign of the current through the junction. Second, the CPR is dominated by a second harmonic, a result of either the presence of transport channels that are out of phase – so called "0" and "π" supercurrent channels – or a Josephson coupling that vanishes in the first order. This asymmetric critical current and dominant second harmonic have been predicted and/or measured in JJs with materials containing ferromagnetism [40, 41, 48–51] or spin-orbit interaction in the presence of a magnetic field [52, 53], d-wave superconductors [45], multiband superconductors [54–59], and topological (p-wave) superconductors [60–63].

Below I detail signatures of BTRS in JJs with weak links of SnTe nanowires, focusing on a critical current which depends on the direction of current flow, an anomalous magnetic diffraction pattern (MDP), and a strong second harmonic in the CPR. These JJs share many of the properties of exotic superconducting junctions. The research I discuss in this Chapter was published in *NPJ Quantum Materials* [64].

My coauthors and I demonstrate how the combined effect of the multiple bands present at the Fermi energy and existence of ferroelectric domain walls in SnTe can explain the two signatures of BTRS in these JJs. Multiband superconductivity and the new Josephson effects can be used to investigate a host of unconventional superconductivity properties including fractional vortices [65, 66], topological superconductivity in multiband materials [67–69], and new types of Josephson-based devices in proximity-induced multiband and ferroelectric superconductors [43, 44].

4.2 Methods

The SnTe nanowires measured in this study were synthesized by metal-catalyzed chemical vapor deposition using a single-zone furnace. SiO_2/Si substrates decorated with 20 nm-wide gold nanoparticles were used as growth substrates. SnTe and Sn source powders were mixed and placed at the center of a horizontal quartz tube with 1-inch diameter while the growth substrates were placed upstream in the quartz tube, 10-13 cm away from the center. The furnace was heated to 600^oC and remained at the temperature for 1hr with an Ar carrier gas at a flow rate of 20 s.c.c.m. The furnace was allowed to cool naturally to room temperature. The resulting samples contained SnTe microcrystals, nanoplates, and nanowires. I characterized the atomic structure and chemical composition by transmission electron microscopy and energy dispersive X-ray spectroscopy. Additional details of the synthesis reactions and microcharacterizations of SnTe nanowires can be found in previous reports [70]. For this study, I selected SnTe nanowires with cross-sectional lengths of $<\sim$300 nm.

The nanowires were examined using transmission electron microscopy (TEM) by P. Liu, H-J Han, M.-G. Han, Y. Zhu, and J. J. Cha, who looked to determine the wires' atomic structure and chemical composition. These experiments were carried out using Gatan's liquid-He cryo holder (HCTDT 3010) and JEOL JEM-ARM200CF at 200 kV at Brookhaven National Laboratory. SnTe nanowires were drop-casted onto Cu-mesh TEM grids overlaid with a thin carbon support film. The TEM sample was cooled from room temperature to 12 K by cooling the cryo holder with liquid helium. The temperature sensor measures the temperature of the holder;

thus, the actual temperature of the sample may be $\sim$ 5–10 K higher.

I fabricated the Josephson devices on $\sim$ 5 mm x 5 mm Si/SiO_2 chips with SnTe nanowires dispersed atop them. First, a pattern of equally spaced alignment marks is written using our lab's Elionix ELS-G100 100 kV Electron-Beam Lithography System with a dose of 1600 $\mu C/cm^2$. After a 60s *in situ* Ar plasma etch at 50 W, I deposited Ti/Au (5 nm/70 nm) using e-beam evaporation. After lifting off the alignment marks, I selected ideal SnTe wires using an optical microscope. Then, I wrote the Josephson devices atop these wires using a dose of 1600 $\mu C/cm^2$. Following development, the samples then underwent a 60 second *in situ* argon plasma etch at 50 W, followed by the sputtering of Ti/Al (4.5 nm/200 nm). To get samples with measurable supercurrents at base temperature, I had to heat the sample during the deposition of aluminum to 100°C.

I carried out low-temperature transport measurements in dilution refrigerators with electron temperatures of < 50 mK. DC electrical leads were heavily filtered to remove high frequency noise above 10 kHz. The lock-in measurements were carried out using a 1 nA excitation at 13 Hz. Radio frequency radiation up to 7 GHz was supplied to one of the electrical leads via a synthesizer through a bias-tee located on the chip carrier.

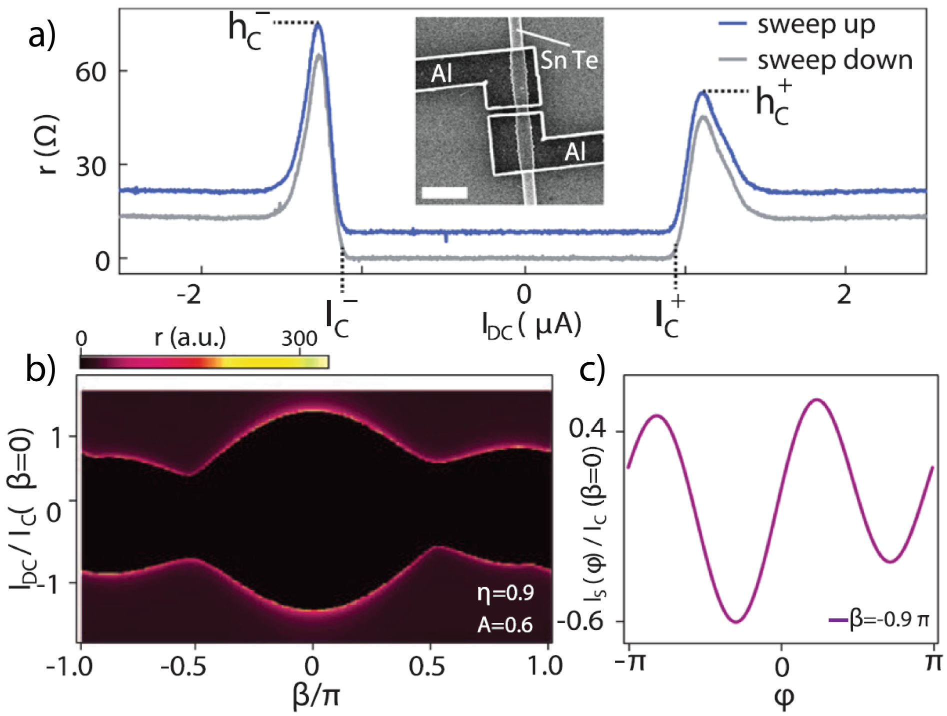

Fig. 4.1: **The DC Josephson Effect for Device 2.** (a) Differential resistance r as a function of DC bias current I_{DC} in different sweep directions. The bias sweeps show no hysteresis and two nonidentical critical currents I_C^+ and I_C^- and peak heights h_C^+ and h_C^-. The curves are offset for clarity. Inset: SEM image of a JJ consisting of two aluminum superconductors coupled via a SnTe nanowire. The white scale bar is 1μm. (b) Simulated differential resistance $r(I_{DC}, \beta)$ calculated from the resistively-shunted junction model, where the best fit of parameters (A, β) are $(0.6, -0.9\pi)$. The resulting CPR is plotted in (c).

4.3 Results and Discussion

4.3.1 Broken symmetry in the DC Josephson effect

I measured the Josephson effect in Device 2, a SnTe nanowire JJ, using lock-in detection of the differential resistance $r = dV/dI$ as a function of the applied DC current (I_{DC}) and AC current (measured in power P). Figure 4.1(a) shows my results in $r(I_{DC})$ at a temperature of $T \sim 25$ mK and $P = 0$. There is no dependence of $r(I_{DC})$ on the direction of current sweep (i.e. there is no hysteresis), indicating the junction is overdamped [24]. Unlike conventional overdamped JJs, I observed different values of I_C for positive (I_C^+) and negative (I_C^-) I_{DC}. Sweeps of I_{DC} in both directions confirmed that the difference in I_C^+ and I_C^- was always present. The measured critical currents $I_C^- = 1.1\ \mu A$ and $I_C^+ = 0.92\ \mu A$ gave a critical current asymmetry of $I_C^-/I_C^+ \approx 1.2$. These sweep-direction-invariant effects are not predicted for conventional JJs [24]. Further, I also measured asymmetric heights of the peaks in r, with the peak larger for I_C^-. The measured peak heights $h_C^- = 65.9\ \Omega$ and $h_C^+ = 45.2\ \Omega$ gave a peak height asymmetry of $h_C^-/h_C^+ \approx 1.46$.

M.T.W. and S.S.K. performed numerical simulations of the resistively-shunted junction model (Fig. 4.1(b)) to determine a CPR that could give rise to this asymmetric critical current. Conventional JJs possess a CPR that is both inversion and π-translation antisymmetric, a result of time-reversal symmetry. We found that the only way to reproduce $r(I_{DC})$ curves that were not symmetric in I_{DC} was to break both of these symmetries: we accomplish this with the CPR $I_S = I_C\left[(\sin(\phi) + \eta \sin(2\phi)\right] + A\left[\sin(\phi+\beta) + \eta \sin(2(\phi+\beta))\right]$. This CPR is comprised of two terms, each containing a first and second harmonic, that are offset by a phase β. The parameter A determines the relative strength of the two terms in the CPR. The parameter η is the strength of the second harmonic terms, which is expected to be significant in the BTRS state for multiband materials [57, 58].

The presence of a strong second harmonic was be confirmed by measuring the AC Josephson effect (see Fig. 4.3) and a value of $\eta = 0.9$ was extracted by comparing these measurements with simulations. Values for A and β were chosen to best match the experimentally determined asymmetries $I_C^-/I_C^+ \approx 1.2$ and $h_C^-/h_C^+ \approx 1.46$: $A = 0.6$, and $\beta = -0.9\pi$. The CPR for these values is shown in Fig. 4.1(c). As expected, it possesses BTRS, i.e. $I(\phi) \neq -I(-\phi)$. The essential feature of this CPR is the two inequivalent minima/maxima, which occur at different values of I_S. It is these features which give rise to the differences in I_C^+, I_C^- and h_C^+, h_C^-.

4.3.2 An anomalous magnetic diffraction pattern

The magnetic diffraction pattern ($r(I_{DC}, B)$) for Device 3 is shown in Fig. 4.2, where B is applied perpendicularly to the sample substrate. Unlike the MDPs of typical Josephson junctions, SnTe JJs displayed a local minimum of the critical current at zero applied magnetic field. The peak in I_C occurs at B=16 mT, which, when using the area of the junction (defined as the junction length plus twice the penetration depth), corresponds to a flux through the device of $\sim \Phi_0/4$ (where Φ_0 is the quantum of flux). This contrasts with magnetic diffraction patterns that have been observed in JJs with weak links of bulk TCIs [22], TIs [26, 71, 72], and strong spin-orbit 1D wires [73], where a maximum in I_C at B=0 is still observed. Our MDPs more closely resemble those for superconductor-ferromagnet-superconductor [74] and d-wave domain wall [75] JJs. Measurements in a parallel field did not produce this effect, ruling out spin-orbit or phase-coherent effects as being the origin of the rise in I_C away from B=0.

I note that magnetic diffraction patterns have previously been observed in JJs with broken time-reversal symmetry. It is interesting to compare the MDP of ferromagnetic JJs [49] with the MDP of our junctions. A minimum at B=0 can be obtained from two supercurrents that are out of phase with each other, consistent with our calculated CPR. For this magnetic diffraction pattern to occur, there must

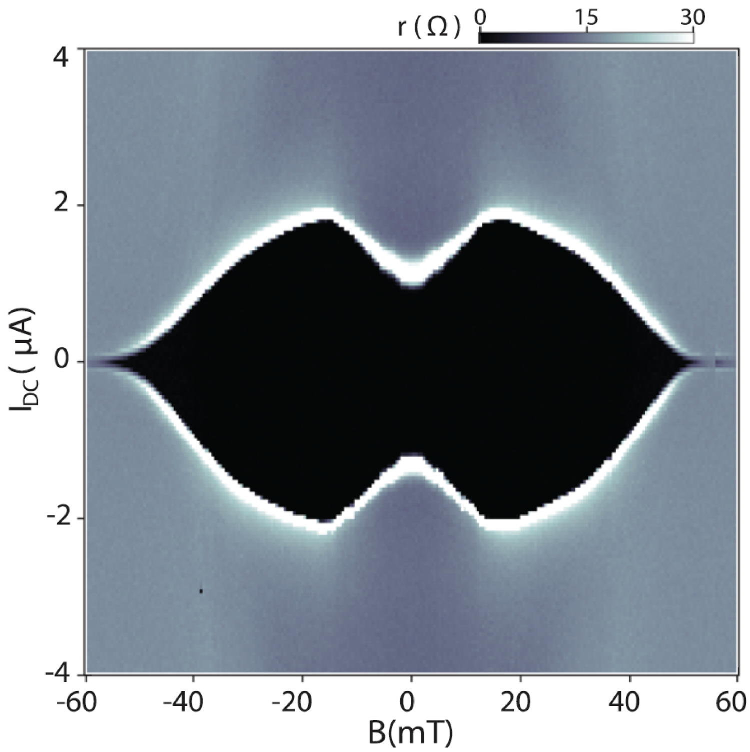

Fig. 4.2: **Magnetic diffraction pattern of a SnTe nanowire JJ (Device 3).**

be some spatial variation along the lateral direction (perpendicular to supercurrent flow) of the magnitude of "0" and "π" supercurrent channels. This can occur, for example, from a lateral variation of the coupling J, or from lateral variations of the chemical potential, or from tunneling coupling near a domain wall. Self consistent calculations of the $s - s^{\pm}$ proximity effect [76] have demonstrated the sensitivity of the dominance of "0" and "π" channels on the chemical potential and tunnel couplings. I will discuss the possible presence of such channels in our samples later in this Chapter.

4.3.3 Strong half-steps in the AC Josephson effect

In this section, I discuss my observations of a modified AC Josephson effect in Device 2. The presence of a second harmonic component – such as in the BTRS state [57,58] – results in additional steps at values of half integer multiples of $hf/2e$. A plot of $r(I_{DC}, P)$ is shown in Fig. 4.3(a), taken at f=5 GHz. In addition to dips in r observed at the expected integer values (labeled in white), prominent features at half-integer values are also apparent. This is more clearly seen in line cuts of Fig. 4.3(a) taken at P=-11.8 dBm (see Fig. 4.3(b). In addition to the dips in r (grey curve) at integer values, clear dips at half integer values also occur. In fact, the drop in r at n = 1/2 is nearly equal to that at n = 1. In addition, the integrated voltage $V = \int ({}^{dV}\!/_{dI}) dI$ versus I_{DC} curve is shown in blue. The plateaus measured in the $I(V)$ curve are nearly equal in strength, consistent with the contributions of the first and second harmonic in the CPR being approximately equal. From this, I extracted a value of $\eta = 0.9$ for the CPR which I used in the numerical simulations shown in Fig. 4.1(b).

The Shapiro diagram shown in Fig. 4.3(a) also has two other signatures that indicate nearly equal contributions from the first and second harmonic terms. First, the width of the zeroth step does not go to zero (indicated by the two white vertical lines), as expected for the zeroth order Bessel function. However, it does go to zero at the next minimum. Second, while the width in I_{DC} of the half integer steps is modulated with power P, including regions of P where the step width goes to zero (as expected), the width modulation is less pronounced on the integer steps. These differences occur for a CPR that has both first and second harmonic terms (see details in simulations in the supplementary information section of Ref. [64]).

Subharmonic steps are expected for underdamped junctions and for overdamped junctions with a skewed CPR. Our junctions are overdamped; hence we

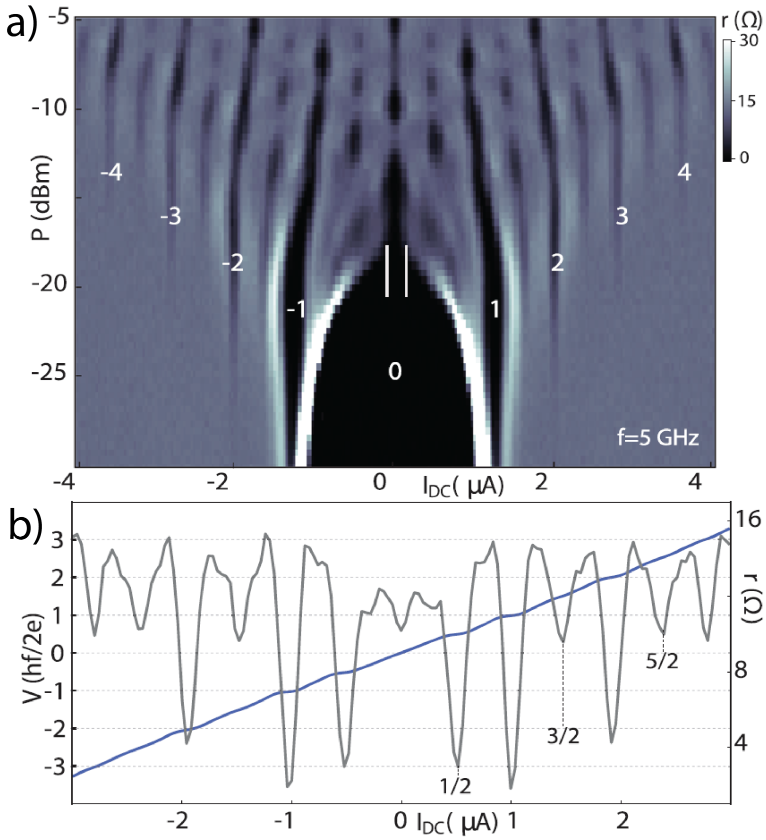

Fig. 4.3: **AC Josephson Effect at ∼ 50 mK.** (a) In addition to integer Shapiro steps, labeled in white, fractional Shapiro steps appear between the integer steps in this false color plot of $r(I_{\mathrm{DC}}, P)$. (b) $r(I_{DC})$ (grey) and integrated voltage $V(I_{\mathrm{DC}})$ (blue) taken at an applied RF frequency f = 5 GHz, P = -11.8 dBm. The first 1/2 integer step occurs with a nearly equal intensity to the first integer step.

do not need to consider the former case. Skewed CPRs in overdamped junctions produce fractional Shapiro steps, but the strength of these steps is typically much reduced compared to the integer steps. For comparison, consider the the AC Josephson effect in $Pb_{0.5}Sn_{0.5}Te$, discussed in Chapter 3. The CPR we used to reproduce this data was that of a ballistic JJ, which has the greatest amount of skewness amongst the likely candidate CPRs. Yet, it produces dips at fractional values that are an order of magnitude smaller than the integer value dips. Therefore, I also ruled out a skewed CPR as the source of the observed effect.

4.3.4 Multiband effect and ferroelectric distortion in SnTe

SnTe is not known to possess ferromagnetic correlations. It has a strong spin-orbit coupling, but the effects observed here are at near-zero magnetic field. Thus, Zeeman splitting or the effects of spin-orbit coupling in magnetic fields cannot explain our observation. Although SnTe is a topological crystalline insulator, as-grown SnTe nanowires have a Fermi energy buried in the valence band [77,78]; hence, transport properties should be dominated by the bulk electronic states. Doped via Sn vacancies, superconducting SnTe has properties that agree well with BCS theory. Yet it has been shown that multiband effects are essential in the description of superconductivity in this material [79].

In my samples, superconductivity arises via the proximity effect, which has a very different character when the proximitized material has multiple bands. Nanowires of SnTe(100) have a rock salt structure that produces two effective bands in the electronic structure of SnTe. Figure 4.4(a) shows an illustration of the proximity effect at the interface between a material with two bands and an aluminum superconductor, with superconducting correlations introduced into each band via couplings J_1 and J_2. In addition, coupling between the bands, J, facilitated by scattering must also be taken into account. When all three couplings are present, the superconducting phase on each band can become unequal. It is at this interface and under the influence of these three couplings that time reversal symmetry is broken.

The proximity effect between an s-wave superconductor and a multiband material shares similarities with a junction between an s-wave superconductor and an

$s\pm$ superconductor. Theoretical investigations of junctions between s-wave and $s\pm$ superconductors have found BTRS [44, 54, 55]. The manifestations of BTRS are two-fold. First is the creation of a canted state (see Fig. 4.4(d)) [54–57], where a nonzero angle forms between the phase of the bands and the phase of the superconductor. Three possible phase angle configurations are shown: for $J \ll (J_1, J_2)$ (see Fig. 4.4(b)), $J \gg (J_1, J_2)$ (see Fig. 4.4(c)) and $J \sim (J_1, J_2)$ (see Fig. 4.4(d)). In the case where $J \gg (J_1, J_2)$ and $J \sim (J_1 = J_2)$, a novel superconducting state is formed. The result of this canting is the generation of chiral currents in momentum space [54,55] – a result of the Josephson currents produced by the difference in phase angle between different bands – and these give rise to BTRS.

This theoretical picture cannot, however, completely explain the results I show in this Chapter. A key discrepancy is that the curve in Fig. 4.1(c) has two minima in r occurring at different values of I_S. These unequal minima are key to replicating the experimental results. Previous theoretical predictions dictate that these two minima be equal, a result of the two phase angle configurations in Fig. 4.4(d) being time-reversal-symmetric partners [55]. Instead, in my system there is a low-temperature ferroelectric distortion that plays an important role, both in creating unequal magnitude in the phase angles in the two bands and because of the phase accumulated when an electron or hole crosses a domain wall between different ferroelectric domains.

The phase angles in the canted state are determined by the coupling via J_1 and J_2 to the Al superconductor, which is in part determined by the density of states at the Fermi energy in the SnTe nanowire. Bulk and thin film SnTe are known

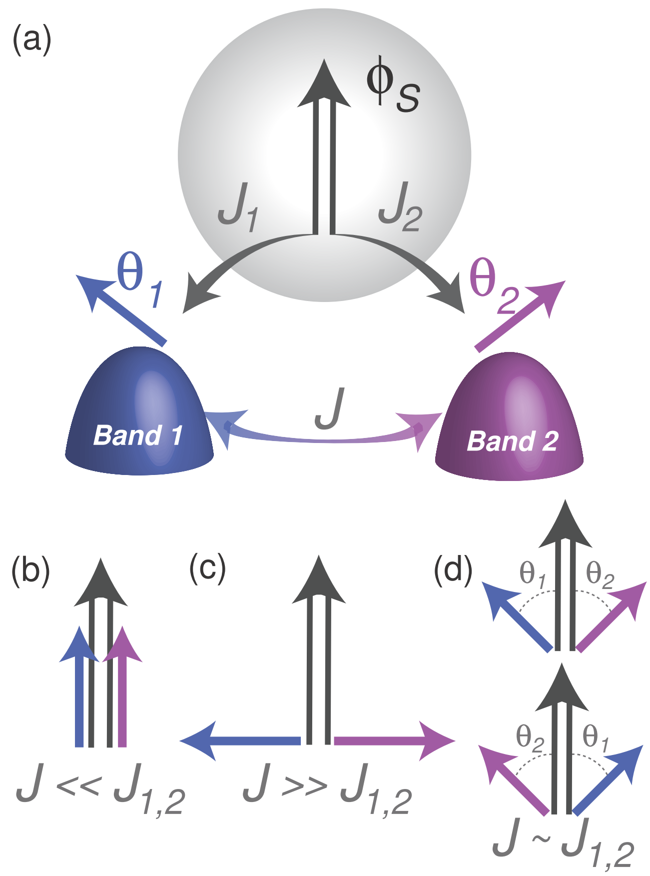

Fig. 4.4: **Proximity effect in a 2-band System.** (a) The two bands in SnTe are coupled to the order parameter with phase ϕ_S in aluminum via an external pairing field for J_1, J_2. The interband coupling J is facilitated by scattering of carriers between bands. θ_1 and θ_2 are the phases of individual order parameters in the two bands. (b-d) The competition between the coupling strengths J and $J_{1,2}$ results in different relative phases between two bands: (b) When $J \ll J_{1,2}$, the phases tend to align with each other. (c) When $J \gg J_{1,2}$, the phases of two bands are out of phase by π. (d) In the intermediate regime $J \sim J_{1,2}$, the phases are canted (shown for the case $J_1 = J_2$). The two degenerate states in the BTRS case are shown.

to undergo a ferroelectric transition at low temperatures, where the cubic phase changes to a rhombohedral phase [80], causing an unequal density of states at the Fermi energy in the two bands of SnTe [81, 82]. Transport measurements of SnTe nanowires have shown kinks in the resistivity curves as a function of temperature, indicative of a ferroelectric transition [77]. It is important to establish the presence of ferroelectric distortion in nanowires, since such a distortion will produce an unequal density of states in each band. The density of states in each band after ferroelectric distortion can be estimated from the electronic density n. Although I could not extract the electronic density n from Hall measurements on nanowires, I can get estimate n from Hall measurements on 2D platelets of SnTe grown under similar condition; this gives n$\sim 10^{21}$ cm^{-3} [77, 78] and a Fermi energy of 330 meV. The ferroelectric distortion pushes one valence band down in energy by 300 meV [82] and both bands are occupied with the relative size of the density of states differing by a factor of ∼3 between the large and small pocket.

To confirm the presence of a ferroelectric distortion, we cooled down SnTe nanowires to 12 K in an *in situ* cryo transmission-electron-microscope (TEM). This allowed us to image the ferroelectric transition and the microstructure of the ferroelectric domains in the SnTe nanowires at low temperature. At room temperature, the SnTe nanowire showed uniform contrast in the bright-field TEM image (see Fig. 4.5(a)); but at 12 K, dark bands appeared along the nanowire perpendicular to the long axis (see Fig. 4.5(b)). These bands were absent at room temperature, and mark walls between two ferroelectric domains that emerge at low temperature. We confirmed this interpretation by examining the electron diffraction pattern from the nanowire. In SnTe, the ferroelectric transition is accompanied by a cubic-to-rhombohedral structural transition. As the nanowire was cooled, the cubic electron diffraction at room temperature changed to show two sets of diffraction patterns, rotated by an angle of $\Delta\alpha$ ∼1.2^{o}, consistent with the two expected ferroelectric domains (see Fig. 4.5(c)). The cubic-to-rhombohedral phase transition occured at 80 K for this nanowire, as all the dark bands suddenly disappeared above this temperature.

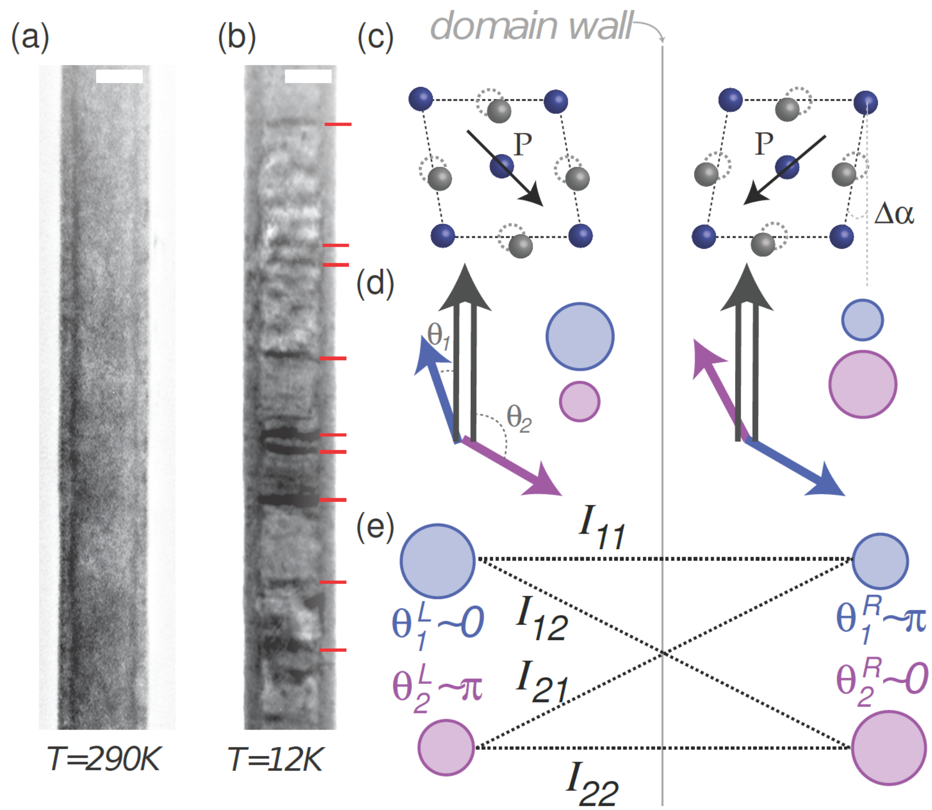

Fig. 4.5: **Effect of Ferroelectric Distortion on Proximity Effect and Josephson Current.** (a-b) TEM images of a SnTe nanowire at T=290 K and T=12 K, respectively. The scale bar in the upper right corner of each image is 50 nm. The dark bands perpendicular to the growth direction, indicated by red lines in (b), are domain walls separating different polarization directions. Scale bars in the upper right corner of each image are 50 nm. (c) The cubic lattice at room temperature undergoes a transition to a rhombohedral lattice at T=80 K with two domains. (d) Unequal phase angles for the two ferroelectric domains. e) The four-channel supercurrent flow across a domain wall. The two interband channels I_{ij} behave like conventional "0"-junctions, while the intraband channels I_{ii} behave like "π"-junctions.

The ferroelectric domain walls are important when considering the supercurrent flow through the JJ. Domain walls between superconducting order parameters are known to cause modifications to Josephson currents. For example, complete destruction of the magnetic diffraction pattern has been ascribed to the coexistence of many energetically degenerate p-wave superconducting domains [47]. Also, motion of the walls between different metastable positions can produce a fluctuating critical current [83–85]. In some SnTe devices, I observed a similarly fluctuating critical current.

In the presence of domain walls, the CPR can be calculated using the phase angles, which can be determined by the proximity effect. There will be four superconducting channels across a wall: two intraband and two interband channels [44, 55]. The four calculated CPRs are $I_{ij}(\phi) = i_{ij}\sin(\phi + \theta_j^R - \theta_i^L)$ for all pairs of $i, j = 1, 2$, where $\theta_{i(j)}^{L(R)}$ are the phase angles of the $i^{th}(j^{th})$ band on the left(right) side of the domain wall and $i_{ij} = 2e\hbar\Delta_i^L\Delta_j^R/m$. Two conclusions can be drawn from a density of states that differs by a factor of ∼3 on the two valleys. First, the valley with the larger pocket will have a phase angle near zero, while the smaller pocket is near π [56, 57]. Hence, $\theta_1^L, \theta_2^R \sim 0$ and $\theta_2^L, \theta_1^R \sim \pi$ (Fig. 4.5(d)), giving rise to two "0" interband ($i \neq j$) and two π intraband ($i = j$) supercurrent channels (Fig. 4.5(e)) [44, 55]. The presence of competing 0 and π channels yields a large second harmonic, consistent with the anomalous magnetic diffraction pattern I observed. Further, we can use the density of states to estimate the magnitude of the proximity-induced superconducting gaps $\Delta_{1,2}^{L,R} = 3\Delta_{2,1}^{R,L} \equiv 3\Delta_0$. The relative magnitude of the "0" and "π" supercurrent components is then: $i_{12} + i_{21} = (2e\hbar/m)(\Delta_1^L\Delta_2^R + \Delta_2^L\Delta_1^R) = 2e\hbar/m(10\Delta_0)$ and $i_{11} + i_{22} = 2e\hbar/m(\Delta_1^L\Delta_1^R + \Delta_2^L\Delta_2^R) = 2e\hbar/m(6\Delta_0)$. The ratio is 0.6. Both the phase and the relative amplitude agree well with the values for A and β obtained from fitting to the AC Josephson data. An additional graphical representation of electron and hole trajectories across a domain wall is shown in Fig. 4.6.

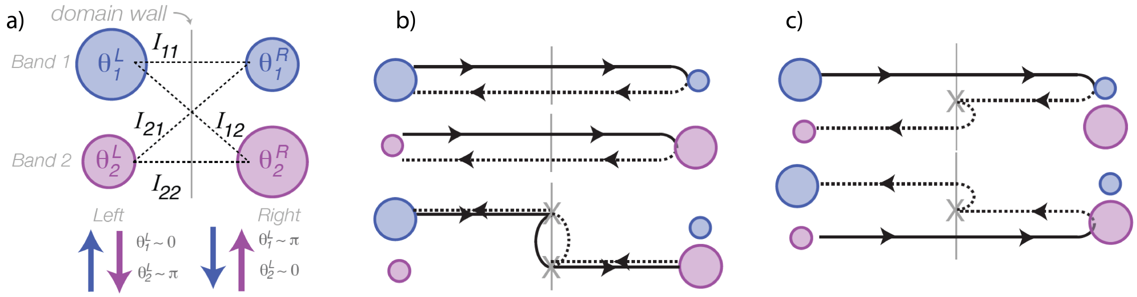

Fig. 4.6: **Electron and hole trajectories across a domain wall.** (a) Four supercurrents present across a domain wall. The lower diagram shows the phase angles on either side, expected when the coupling to one band is stronger. (b-c) A comparison of electron/hole trajectories across the domain wall. Bands 1(2) are indicated in blue(purple) and the size of the circle indicates the density of states at the Fermi level. Electron(hole) trajectories are shown in solid(dashed) lines, and arrows indicate the direction of propagation. (b) For trajectories which involve no interband scattering at the domain wall or an even number of scattering events, no net accumulation of phase occurs at the wall. Hence, supercurrents generated by these trajectories produce a CPR with no phase offset. (c) For an odd number of scatterings, a net phase is accumulated for transport across the domain wall.

4.4 Conclusion

In summary, in Chapter 4 I discussed my measurements of the combined effects of proximity-induced multi-band superconductivity and ferroelectric distortion on the dynamic properties of JJs made from SnTe nanowire weak links. I described my observations of four unusual JJ behaviors – the asymmetric critical currents, asymmetric peak heights, a strong second harmonic and an anomalous magnetic diffraction pattern – within the theoretical framework. I note that ferroelectric distortion offers new possibilities for controlling the flow of supercurrents, where modification of the density of states or ferroelectric transition temperature by electric fields and strain can be used to modulate the supercurrent and the offset phase in the device. The manifestation of multiband and multicomponent superconductivity in our devices offers experimental access to the phase induced on individual bands.

This may allow future investigations of the order parameter in novel superconductors [43,44] and the determination of topology in the superconducting state [67–69].

Chapter 5: Modifications to the AC Josephson Effect Observed in Josephson Junctions with Weak Links of $(BiSb)_2Te_3$

The contents of this chapter are under review at *Physical Review X*. The arXiV preprint of this work can be found in Ref. [86].

5.1 Introduction

The surface of a three-dimensional topological insulator hosts a non-degenerate band of massless Dirac fermions [87]. Proximity to an s-wave superconductor is predicted to mediate $p+ip$ pairing in the topological surface state, a consequence of the spin texture of the Dirac band. A Josephson junction with a TI weak link should support gapless Andreev bound states (ABSs) that are one-dimensional Majorana fermions [88]. Majorana bound states (MBSs) would impart a 4π-periodic component to the junction's current-phase relationship, which would coexist with the 2π-periodic component from the spectrum of conventional ABSs at higher energies. In principle, 4π periodicity can be detected via the fractional AC Josephson effect: the junction current oscillates at half the normal Josephson frequency for a given voltage, or, equivalently, DC junction voltage is twice as large for a given frequency of AC current. Because of this, under radio frequency (RF) irradiation, the MBSs will comtribute to Shapiro steps at $V = nhf/2e$ for only even n.

Claims for the observation of the fractional AC Josephson effect have been made in a variety of topological systems, including nanowires with spin-orbit coupling [89, 90], strained 3D HgTe [91], 2D HgTe [92, 93], Dirac semimetals [94], Bi_2Se_3 [95], and Bi_2Se_3 [96, 97]. Among these works, only in 2D HgTe has suppression of odd Shapiro steps beyond the first been observed [92]. Suppression of the first Shapiro step, however, can result from trivial effects in Josephson junctions, including Joule heating [95] and underdamping [98]. Therefore, the suppression of higher odd Shapiro steps is a crucial step in eliminating the ambiguity surrounding claims of 4π periodicity. In addition, Landau-Zener transitions (LZTs) can suppress the expression of the first and higher odd Shapiro steps, but only in devices with near-unity interface transparency between superconductor and weak link [99]. This offers a possibly clear-cut way to rule out this mechanism.

Fabricating high-quality Josephson junctions with TI weak links is technically challenging. A number of groups have demonstrated superconducting contact to exfoliated flakes from single crystals of Bi_2Se_3-class topological insulators [100–107]. Yet even were Majorana physics confirmed, lack of scalability and reliable reproducibility of the exfoliation process would limit the impact of that approach. A thorough study will require statistical analysis of data from many devices. Similarly, the technological goal of a scalable topolgical quantum computing architecture based on Majorana fermions, will require the presence of Majorana modes in a TI film grown at wafer scale by molecular beam epitaxy (MBE) or another suitable technique. Progress in MBE-based platforms has been hampered by poor superconductor/TI interface quality and the difficulty in protecting fragile Bi_2Se_3-class films during device fabrication.

In this Chapter, I discuss lateral Josephson junctions that the Goldhaber-Gordon group fabricated through the self-formation of a superconducting Pd-Te layer, as pioneered by Bai et al [108]. Using a variety of imaging techniques and low-frequency electrical measurements, I show that this fabrication process yields a superconductor/TI interface with moderate transparency, while minimizing damage to the TI film and approximately matching the work-function between the superconductor and the TI. Under radio-frequency (RF) excitation, I observed suppression of the 1st and 3rd Shapiro steps in one device, and suppression of the 1st step in other devices. However, some devices showed continued Shapiro step behavior. I argue that these observations are not the result of Landau-Zener transitions or junction hysteresis, but do support the presence of Majorana bound states in the junctions. Further theoretical exploration of non-equilibrium effects in these systems is needed to understand what other effects may be present, particularly in light of the variation in results among similar devices.

5.2 Methods

Two challenges must be overcome to develop superconductor/TI heterostructures: achieving sufficient electrical transparency of the interface and preserving the topological character of the TI. Both must be solved to observe Majorana physics. The former, a well-known problem from superconductor/semiconductor structures [109–113], is required to achieve a pairing gap in the topological surface states via the proximity effect. The latter problem is specific to topological matter, and is particularly difficult due to the susceptibility of Bi_2Se_3-class materials to unwanted doping; a TI's Fermi level must lie within the bulk bandgap so that the topological surface states are not shunted by trivial bulk states. In MBE-grown films, the Fermi level is commonly tuned by adjusting the composition of ternary $(Bi_xSb_{1-x})_2Te_3$ (BST) and quarternary $(Bi_xSb_{1-x})_2(Se_yTe_{1-y})_3$ alloys, compensating for charged disorder including Te vacancies, Sb-Te anti-site defects, and interfacial defects [114–116]. However, fabricating devices from such films can introduce additional disorder, destroying the delicate charge balance or introducing mid-gap defect states. Furthermore, charge transfer from the superconductor can substantially dope the TI, unless the work functions of the two are closely matched.

Two recent developments have enabled highly transparent superconductor/TI interfaces and, in turn, realization of the Josephson effect in MBE-grown TI films. One approach is to grow the TI and superconductor structures entirely *in situ* using stencil lithography to facilitate patterning. This approach led to the observation of a suppressed first Shapiro step [96]. Here, I describe a second approach: the self-formation of a superconducting Pd-Te layer using laterally-patterned *ex situ* deposition of Pd [108]. Although chemical reactions with deposited metal can be problematic [117] (for example, depositing Al on Sb_2Te_3 might create a barrier layer of AlSb, a ~ 2 eV bandgap semiconductor), here the reactivity between Pd and Te is desired.

Our devices were based on an 8 quintuple layer thick $(Bi_{0.4}Sb_{0.6})_2Te_3$ (BST) film grown by MBE on a GaAs substrate. We patterned PMMA e-beam resist masks for Josephson junctions using a low-voltage electron beam lithography process developed to impart minimal beam damage to the TI film. The lateral Josephson junctions were fabricated by depositing 11 nm Pd on a resist-masked BST film in an electron beam evaporator, forming a superconducting Pd-Te alloy (with residual Bi and Sb) in exposed regions, while the BST weak link was masked. After depositing the Pd and performing liftoff, we etched away unwanted areas of BST by Ar ion milling. In some devices, the etched region abutted the Josephson junction weak link, terminating its transverse extent. In other devices, a region of BST film surrounding the weak link was left unetched. We noticed no difference in electronic transport. Our methodology and the junction geometries are described further in the supplementary materials of Ref. [86].

The junctions had geometric lengths of roughly $L = 160$ nm (parallel to current flow; measured by scanning electron microscopy) and width $W = 2$ µm (transverse to current flow). Throughout this Chapter, critical temperatures, fields, and currents are defined by the condition $R = R_N/2$, where R_N is the normal state resistance. We determined the critical temperature and field of the superconductor by transport through a strip of the superconductor with no weak link. All of the devices discussed in this chapter were fabricated simultaneously on the same chip.

5.3 Results and Discussion

5.3.1 Device characterization

The electronic characteristics of the BST film were determined by Hall measurements at 30 mK. We found the film's sheet resistivity to be $\rho_{xx} = 1.55$ kΩ. The conductivity was due to n-type charge carriers with density $n = 4.8e12$ cm^{-2}, with mobility $\mu = 820$ cm^2/Vs and elastic mean free path $\ell_e = \hbar k_F \mu/e = 15$ nm. The film had negative magnetoconductance, indicating weak anti-localization [118, 119]. Fitting the magnetoconductance by the Hikami-Larkin-Nagaoka formula yielded a phase coherence length $\ell_\phi = 850$ nm [120], which we used to estimate the inelastic mean free path ℓ_i.

A cross-sectional image of a portion of a junction taken in a transmission electron microscope, is shown in Fig. 5.1(b). The deposited Pd diffused vertically through the entire $(Bi_xSb_{1-x})_2Te_3$ film and into the GaAs substrate. Excess Pd formed grains on top of the film. Pd diffused laterally into the weak link by roughly 40 nm. These findings were confirmed via energy-dispersive x-ray spectroscopy, x-ray photoelectron spectroscopy, and scanning Auger electron spectroscopy.

Since Pd diffused through the full vertical extent of the film, regions where Pd had been deposited had no remaining topological insulator layer. The direction of current flow at the edge of the weak link would therefore be normal to the superconductor/TI interface. I note that this geometry differs from that of junctions based on deposited elemental superconductors, which sit atop the topological insulator and have current flow along the interface plane.

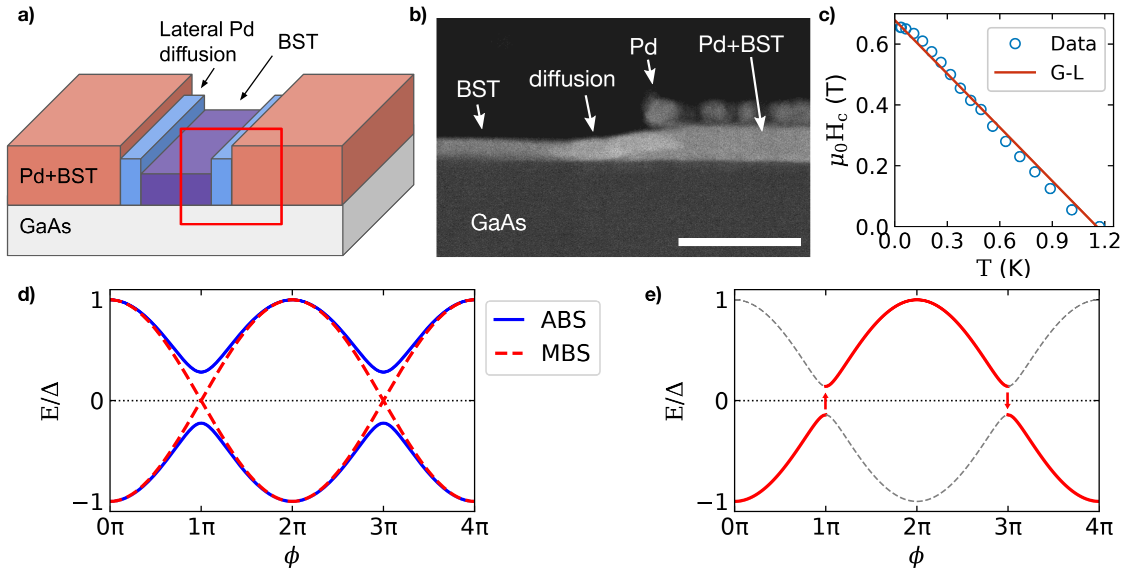

Fig. 5.1: **Junctions with a self-formed Pd-Te superconductor.** (a) Schematic of a junction (not to scale). The superconductor/TI interface is lateral, unlike most SN junctions, where the superconductor sits on top of the normal metal. At the interface is a region where Pd diffuses laterally into the weak link. (b) Cross-sectional high-angle annular dark-field (HAADF) TEM image of a portion of a junction indicated by the red box in (d). At left, the BST weak link. At right is the superconducting Pd-Te region, with greater film thickness due to Pd incorporated into the BST. Excess Pd has formed grains atop the film. At center, Pd has diffused laterally into the weak link by about 40 nm. Scale bar, 50 nm. (c) Out-of-plane critical field H_c versus temperature T of the Pd-Te superconductor (blue circles), and a fit (red line) to Ginzburg-Landau theory for out-of-plane field. (d) The spectrum of an ABS (blue line), with 2π periodicity, and a MBS (red dashed line), with 4π-periodicity. (e) An excitation (red line) traversing a 2π-periodic ABS (grey dashed line) as the phase ϕ across the junction evolves, with LZTs (red arrows) at $\phi = \pi$ and 3π, imparting a 4π-periodic component to the current-phase relationship.

Many superconductors have work functions substantially offset from that of Bi_2Se_3-class materials. For example, the work functions of bulk Al and Nb are less than that of Bi_2Se_3 by nearly 1 V [121, 122]. Moreover, the difference exceeds the 0.3 eV bulk bandgap of Bi_2Te_3. At a transparent interface between these two materials, charge transfer should dope the TI, moving the chemical potential into the bulk conduction band and enabling topologically trivial Cooper pairing. Using Kelvin probe force microscopy (KPFM), we confirmed that the work function of evaporated Al is offset from that of BST by -880 meV.

The work functions of Pd and Pd-Te alloys are substantially closer to that of Bi_2Se_3-class materials. We found that the work function of Pd-Te exceeded the work function of the BST film by roughly 200 meV, a significantly smaller offset than from elemental superconductors. The supplementary material for Rosen et al [86] contains further details regarding the KPFM measurements.

The Pd-Te superconductor has critical temperature $T_c = 1.17$ K, normal state sheet resistivity 100 Ω/sq, and critical field $\mu_0 H_{c2} = 655$ mT (Fig. 5.1(c)). From this I find a coherence length $\xi = 22.4$ nm through the Ginzburg-Landau relation $\xi^2 = \frac{\Phi_0}{2\pi H_{c2}}$. The devices therefore fall in the long dirty junction limit for which $\xi, \ell_e \ll L$.

5.3.2 Device 4: Observation of a fractional AC Josephson effect

The current-voltage relationship of Device 4 is shown in Fig 5.2(a). Supercurrent flows across the junction below the critical current $I_c = 370$ nA. At higher currents the differential resistance reaches the normal state resistance $R_N = 146\ \Omega$. Extrapolating the normal section of the current-voltage relationship to zero voltage yields an excess current $I_e = 136$ nA, as expected for a high transparency weak link. Although the Pd-Te superconductor may not be well described by BCS theory, if we take the superconducting gap as $\Delta_{\mathrm{BCS}} = 1.76 k_B T_c$ we arrive at the dimensionless figures of merit $eI_cR_N/\Delta_{\mathrm{BCS}} = 0.30$ and $eI_eR_N/\Delta_{\mathrm{BCS}} = 0.10$; naively, the latter implies a junction transparency $\tau \approx 0.25$ according to BTK theory [123]. Device 5 had $eI_eR_N/\Delta_{\mathrm{BCS}} = 0.29$, implying $\tau \approx 0.3$ The current-voltage relationship is not hysteretic, indicating that the junction is overdamped (consistent with our estimation of the Stewart-McCumber parameter $\beta_C \sim 10^{-4}$) and that Joule overheating is not limiting the retrapping current [124].

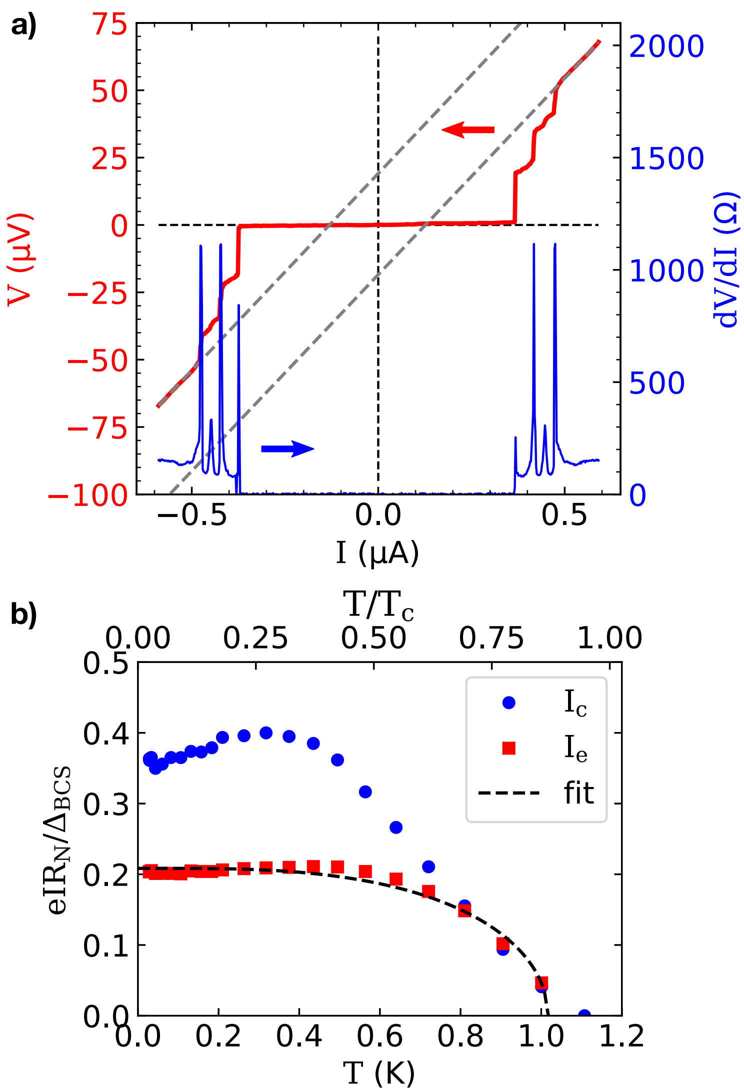

Fig. 5.2: **Junctions with Pd-Te superconducting leads under DC bias.** (a) Voltage (red) and differential resistance (blue) of Device 4 as a function of current bias I. (Dashed lines) Linear fits at high bias. The excess current is determined by the intercept of these lines with $V = 0$. (b) Critical current and excess current of Device 5 as a function of temperature. (Dashed line) The temperature dependence of the BCS superconducting gap fit to the excess current.

Figure 5.3 shows the resistance versus current of Device 4 in a perpendicular magnetic field. The critical current displays the typical Fraunhofer pattern, approaching zero at nonzero integer multiples of magnetic field $B_0 = \frac{\Phi_0}{L_{\text{eff}} W}$, where L_{eff} is the effective junction length and W is the width. A fit yields $L_{\text{eff}} = 1.1$ μm, which is significantly larger than the geometric length of the junction $L \approx 160$ nm. We found this disparity surprising, as we expect minimal flux focusing by the narrow Pd-Te leads.

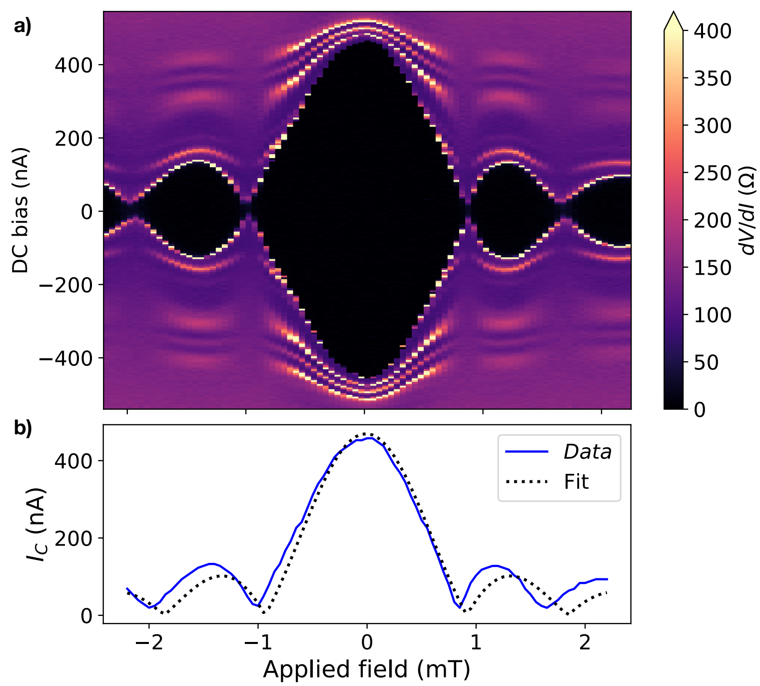

Fig. 5.3: **Device 4 in a perpendicular magnetic field.** (a) Differential resistance at finite bias. (b) The extracted critical current. (Dashed line) Fit to the Fraunhofer pattern.

The differential resistance of Device 5 is shown in Fig. 5.4 under an additional radio-frequency (RF) drive at frequency $f = 4.3$ GHz. Outside of the central zero-resistance region at low bias and low RF power are a series of regions of low differential resistance at finite DC voltage. These regions are centered at voltages $nhf/2e$ for integer n, as expected for nth Shapiro steps. I note that the strengths of the differential resistance dips associated with the 1st and 3rd Shapiro steps are suppressed relative to those of the 2nd and 4th steps.

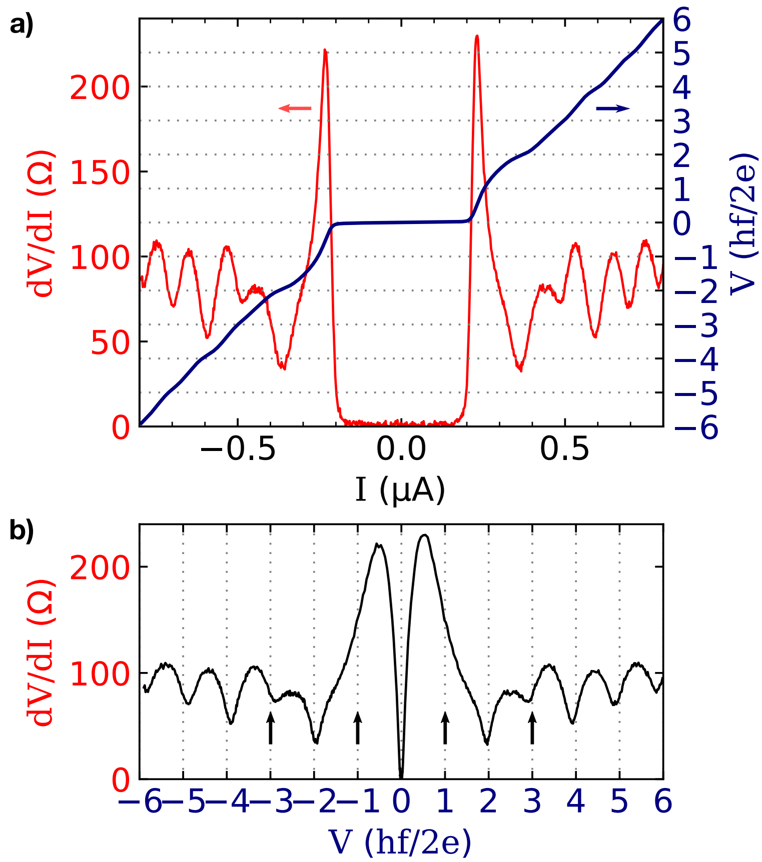

Fig. 5.4: **Current-voltage relationship in Device 5 under 4.3 GHz excitation (nominal power -33.5 dBm).** (a) (Left) differential resistance versus current bias, and (right) DC voltage, obtained by numerical integration of the differential resistance. (b) The same data shown parametrically, emphasizing the suppression of the first and third Shapiro steps (arrows).

The evolution of the differential resistance with RF excitation power in Device 5 is shown at different RF frequencies in Fig. 5.5(a-c). The development of Shapiro steps is shown more clearly by the false color plots in in Fig. 5.5(d-f), which were formed by grouping the data points (equally spaced in DC current) into DC voltage bins; the voltages where steps occur are visible as bright horizontal streaks. At 4.3 GHz, the weights of the 1st and 3rd Shapiro steps are suppressed at low powers in comparison to those of the 2nd and 4th steps, and develop only at higher powers. The 3rd step is recovered as the RF frequency is increased to 5.7 GHz, as is the 1st step at 10 GHz.

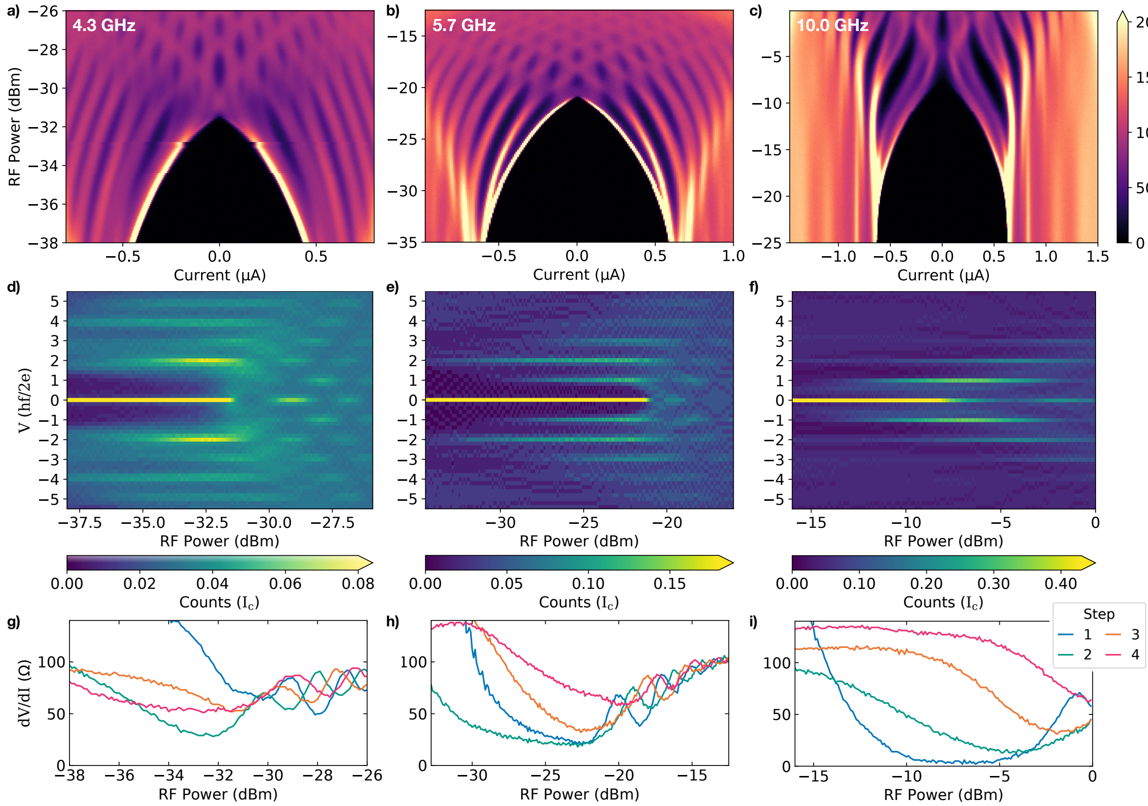

Fig. 5.5: **Shapiro steps in Device 5.** (a-c) False color plots of the differential resistance as a function of bias current and RF excitation power. (d-f) Corresponding histograms of measured points within DC voltage bins, shown in normalized units $hf/2e$, with the number of counts in each bin normalized as a fraction of the critical current. The nth Shapiro step appears at voltage $nhf/2e$. (g-i) The value of the differential resistance at the 1st through 4th Shapiro step, as a function of RF power. The frequency of RF excitation is (a, d, g) f =4.3 GHz, (b, e, h) 5.7 GHz, and (c, f, i) 10 GHz.

Suppression of odd Shapiro steps is an expected signature of the presence of a MBS. The ABS spectrum of a conventional Josephson junction is 2π-periodic, leading to a 2π-periodic current phase relationship and Shapiro steps at voltages $V = nhf/2e$ for integer n. The 2π-periodicity results from an avoided crossing of the two branches of the lowest-energy ABS at $\phi = \pi$ (see Fig. 5.1(d)), a consequence of scattering in the junction or at interfaces. However, contacting a TI to a superconductor is expected to induce effective p-wave pairing [88], and a junction between

p-wave superconductors should support a pair of Majorana bound states [125–127]. At $\phi = \pi$ and 3π, the two Majorana bound states do not couple and are therefore at zero energy (see Fig. 5.1(d)). Because these states differ in fermion parity (unlike ABS, which tunnel charge $2e$), this picture should be valid provided the Majorana modes are spatially separated and there are no quasiparticle excitations [128], requiring $k_B T \ll \Delta_{\mathrm{BCS}}$.

Device 5's current-phase relationship should possess a 4π-periodic component, which coexists with the 2π-periodic term [129]. At high RF power and frequency, the 2π component is expected to dominate, but at low RF power and frequency, the 4π component may dominate, leading to a suppression of Shapiro steps with odd n [95].

I should clarify that my observation of suppressed odd Shapiro steps does not necessarily imply the presence of a Majorana mode. The lowest Shapiro steps can be suppressed at low RF power in underdamped junctions [98], as well as in overdamped junctions if there is self-heating [130, 131]. The small capacitance and apparent lack of hysteresis in our junctions is not consistent with these effects; furthermore, these effects cannot suppress the third step while leaving the second step intact. Another possibility is suppression of the first and third Shapiro steps due to Landau-Zener transitions (LZTs) between upper and lower ABS branches near $\phi = \pi$ (Fig. 5.1(e)). This was predicted [132, 133] and recently observed in a lateral Josephson junction made with a topologically trivial InAs weak link [99], with a high interface transparency. The probability of an LZT is

$$P = \exp\left(-\frac{\pi(1-\tau)\Delta}{eV}\right), \tag{5.1}$$

which is significant only when $\tau \approx 1$ [134]. Our junctions have an estimated $\tau \sim 0.3$, far from the high-transparency regime in which LZTs occur.

While we have ruled out hysteresis and LZTs as the source of the suppressed Shapiro steps, the possibility of other effects needs to be considered. Recent computational work suggests that the nth Shapiro step can be suppressed or obscured by unwanted device resonances if the resonances occur at DC voltages at or near $nhf/2e$ [135]. This obvious effect does not explain our results, as we observe suppression of the 1st and 3rd steps only, and suppression of the first step is seen throughout the range 2.5 GHz (the lowest frequency at which Shapiro steps clearly develop) to 7 GHz. On the other hand, we did indeed observe strong resonances above the critical current in our devices. The resonances appear at fixed voltages with varying field and temperature, even close to T_c, which is inconsistent with multiple Andreev reflection and Fiske resonance. Instead, we suggest they come from simple radiative coupling of the device to cavity resonances of the wiring. Because these resonances are cryostat-specific, reproduction of our results in other cryostats could exclude the possibility that the suppression of Shapiro steps is related to these resonances (I note that the DC characterization was performed in a different cryostat than measurements under RF irradiation).

A potential drawback of our devices is the relatively short coherence length of the Pd-Te superconductor, which places our devices in the long junction limit $\xi \ll L$. We attempted to bolster the superconducting coherence lengths of the junction leads on a test device by evaporating 65 nm Al immediately after depositing 5 nm Pd on the BST film. The hybrid Al/Pd-Te superconductor had a critical temperature of 780 mK (whereas evaporated Al films alone had a T_c of roughly 1.3 K), and a critical field of 13 mT. Compared to junctions with Pd-Te alone, junctions with hybrid superconducting leads had similar low-frequency transport characteristics, although somewhat lower critical currents and excess currents (in some devices, $I_e < 0$).

Since we expected the coherence length to be increased in the Pb-Te-Al superconductor, but the junction length was unchanged, the junctions should support fewer trivial ABS [136] coexisting with the single MBS. We therefore expected a proportionally larger 4π-periodic component, leading to more prominent suppression of odd Shapiro steps. Instead, we observed all Shapiro steps in all measured devices. Furthermore, in some devices, Shapiro steps at fractional multiples of $hf/2e$ were observed. Shapiro steps at multiples of $hf/4e$ have been seen in junctions with exceptionally high transparency [137], reflecting the skewed current-phase relationship in this regime [29]; yet our devices appear to have had substantially lower transparency. Further work is needed to understand whether these steps reflect higher harmonics of the current-phase relationship or other resonance effects in the devices. These results further highlight the complexity of non-equilibrium processes in the excitation spectra of these devices and the complicated behavior of superconducting tunneling.

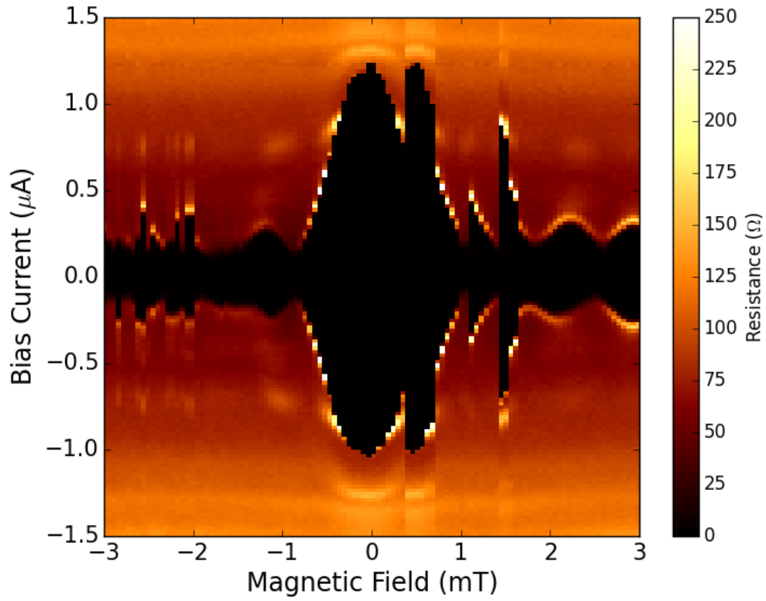

Fig. 5.6: **Magnetic diffraction pattern for Device 6.** Fraunhofer-like magnetic diffraction pattern, which shows evidence of flux trapping.

5.3.3 Device 6: Probabilistic distortions to the AC Josephson effect

In this section, I discuss my measurements of Device 6, another $(BiSb)_2Te_3$ device. This device showed unusual features revealed in Shapiro diagrams. Device 6 was approximately 2 μm long and 80 nm wide, as determined by SEM.

Figure 5.6 shows Device 6's fraunhofer-like diffraction pattern, which is expected for a long junction with a supercurrent that is uniform spatially across its width. As the Figure shows, I observed a pattern with clear openings and closings of the superconducting lobes. However, the magnetic pattern was affected by what I suspect to be flux trapping in the leads, which causes inconsistent changes in the critical current I_C as the applied field is swept. Additionally, I found no field at which I_C was suppressed completely to zero.

When Device 6 was subjected to RF irradiation, several interesting featured

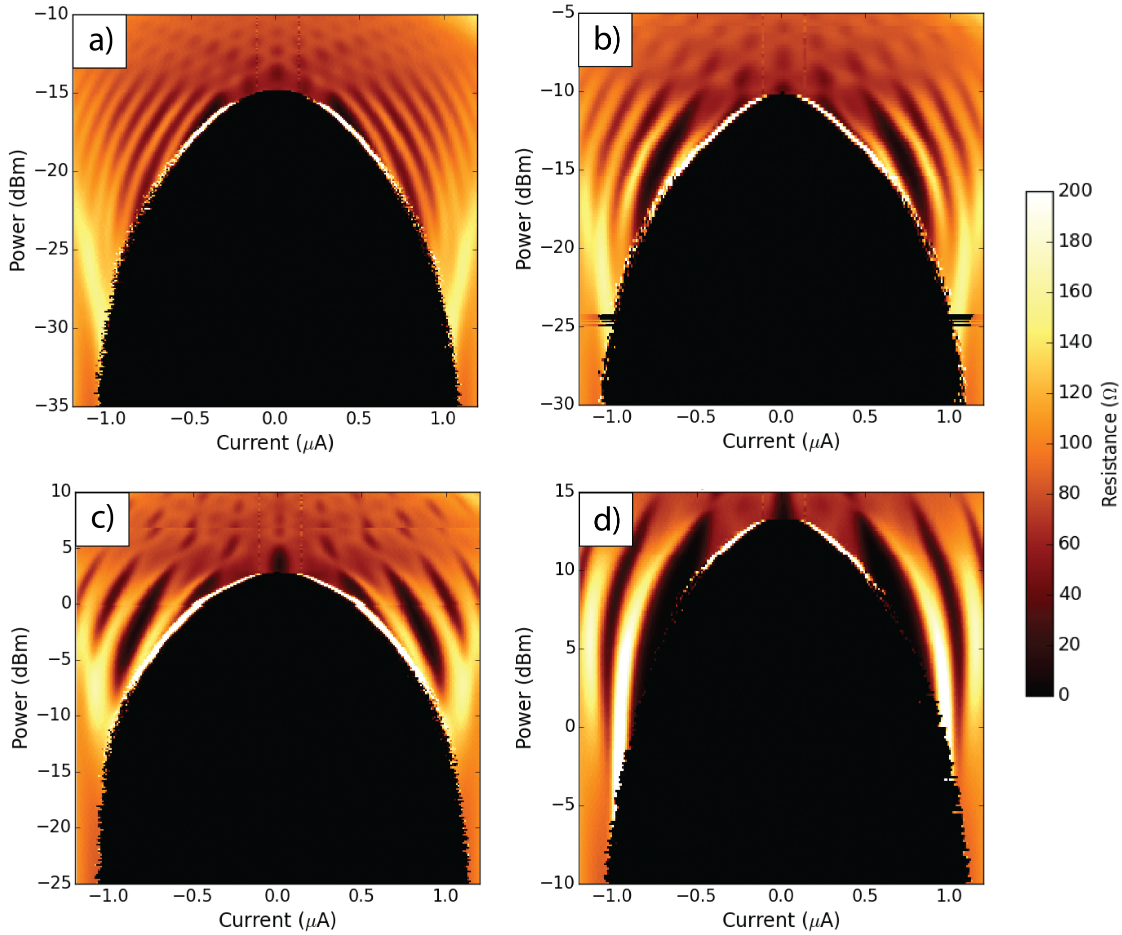

Fig. 5.7: **Shapiro maps at 57 mK for Device 6.** (a) With excitation frequency of 4.5 GHz, (b) 7 GHz, (c) 9 GHz, (d) 12 GHz.

appeared, including fuzzy or irregular switching transitions from the zero-voltage state, "feathering", and symmetrical distortions, which were especially prominent on the zero step. Representative Shapiro maps showing each of these features are shown in Fig. 5.8.

First I will discuss the jagged or "fuzzy" edges that can appear on the zero step boundary, which can be seen in all of the maps in Fig. 5.7. This feature is highlighted in Fig. 5.8(a), which shows a more detailed image of the map in Fig. 5.7(b). Irregular transitions from the zero-voltage state to the nonzero-voltage state may be due to a probabilistic tunneling process. Macroscopic quantum tunneling–

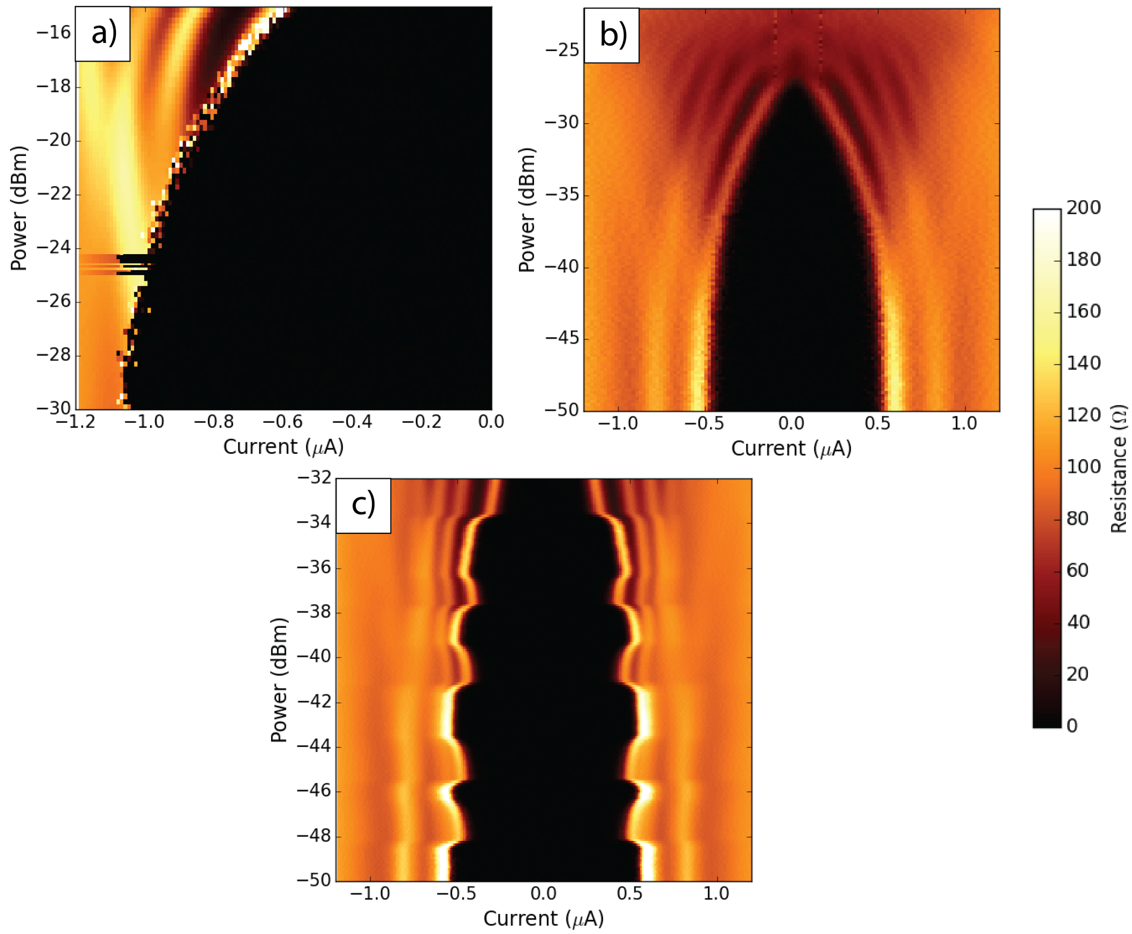

Fig. 5.8: **Interesting emergent features.** (a) zoomed in image of Fig. 5.7(b), showing the "fuzzy" step edges [at 7 GHz, 57 mK, 0 mT]. (b) "Feathered" step edges [at 4.3 GHz, 460 mK, 0.36 mT]. (c) broad symmetrical distortions to the pattern [at 4.3 GHz, 500 mK, 0.36 mT].

where a phase particle in the tilted washboard potential tunnels through one of the potential's barriers–could explain these fuzzy step edges, but this still leaves the question of whether this mechanism would occur in junctions that fit the parameters of our devices.

Next, I saw that "feathering" of step edges sometimes occurred (see Fig. 35.8(b)). We are uncertain what might cause this effect. Lastly, in some cases, we observed symmetrical distortions to the Shapiro pattern. These may be subtle, or dramatic like those shown in Fig. 5.8(c), but they were always symmetrical with respect to $I_{DC} = 0$ and affected the zero step more strongly than other steps. I never observed this effect at base temperature (~50 mK), but rather it became apparent as the temperature was increased, and was sometimes strengthened further by the application of a small magnetic field. For example, the map in Fig. 5.8(c) was measured at 500 mK, with a perpendicular field of 0.36 mT. The distortions in this figure are some of the strongest we were able to observe; however, a variety of maps we collected at other temperatures and RF frequencies also showed this effect.

It is important to note that none of these unusual features reoccurred exactly upon a repeat of the same measurement. For example, one may compare the maps in Figs. 5.8(b) and 5.8(c), which were taken under similar conditions, yet produced substantially different looking Shapiro diagrams. Because of the probabilistic nature of these disruptions, a modified or unconventional CPR would not be sufficient to explain the effects. It seems unlikely that these features can be captured within the framework of the RCSJ model without the inclusion of some external disturbance or additional physics.

5.4 Conclusion

In this Chapter I discussed the fabrication of Josephson junctions with topological insulator weak links using self-formed superconductors. The devices showed good interface transparency while with little apparent damage to the TI. I observed suppression of the first and third Shapiro steps under low power and low frequency RF excitation, a hallmark of a fractional AC Josephson effect that is consistent with the existence of Majorana bound states: topologically protected gapless Andreev bound states. To the best of my knowledge, our data is inconsistent with topologically trivial sources for the suppression of Shapiro steps, and presents the strongest evidence to date of 4π periodicity, aside from that in 2D HgTe quantum wells.

However, our difficulty in obtaining reproducible results between devices, and the lack of suppression of odd Shapiro steps in devices with hybrid Al/Pd-Te superconductors, casts doubt upon such an interpretation. More work is needed to understand how the structure of the superconductor/TI interface influences Andreev spectra and whether our observations of suppressed Shapiro steps reflect 4π periodicity or its mimicry by other nonequilibrium effects. Provision of full data sets, with commentary but not post-selection, is needed for the community to reach reliable conclusions regarding the existence of Majorana modes. This work was under review at *Physical Review X* at the time this was written.

I also presented an RF data set from a single device that produced unusual, varying features in its Shapiro maps. These features included jagged step edges, "feathered" step edges, and prominent symmetrical distortions to the zero step, all of which may indicate the existence of other physics being important. Understanding the connection between this device and the others we have studied may provide more clarity on nonequilibrium effects within our devices, and on the circumstances under which Shapiro steps are suppressed in this material.

Chapter 6: Conclusion and Outlook

In this dissertation, I briefly reviewed the physics of Josephson junctions and topological materials, and then discussed my experimental investigations of three non-standard Josephson effects in junctions made from weak links of different topological materials.

In Chapter 3, I presented my measurements of the AC Josephson effect in $Pb_{0.5}Sn_{0.5}Te$ JJs, in which I observed rich subharmonic structure. In comparison, I observed conventional results in junctions made from the similar but trivial material PbTe. From this data and simulation I showed that the CPR of the $Pb_{0.5}Sn_{0.5}Te$ junctions was consistent with a CPR that was a maximally skewed sinusoid. The form of this CPR implied topologically-enabled unity transparency in the weak link, which we ascribed to 1D helical edge modes.

Similarly, in Chapter 4 I discussed my measuremebts of the Josephson effects in SnTe nanowires. I found that the proximity-induced superconductivity in the wires exhibited an unexpected breaking of time-reversal symmetry. I discussed three experimental observations that led to this conclusion: an asymmetrical critical current in the DC Josephson effect, a prominent second harmonic in the AC Josephson effect, and an anomalous magnetic diffraction pattern that showed a minimum in critical current at zero magnetic field. I proposed a functional form for a CPR that reproduced these features, and I described how multiband superconductivity and ferroelectric domain walls might give rise to these effects.

Finally, in Chapter 5 I discussed my measurements on JJs made with weak links made of $(BiSb)_2Te_3$. Under RF irradiation, at low power and frequency, I observed suppression of the first and third Shapiro steps in one device. In other devices, I found suppression of only the first Shapiro step. I discussed how these observations are consistent with 4π periodicity in the junction's CPR – a hallmark of Majorana bound states – but inconsistent with other topologically trivial mechanisms that can suppress steps. Since the Shapiro maps of different devices showed great variation, more data from more devices will be necessary to fully understand the nature of the Josephson effect in this material – and whether Majorana modes might be present.

Bibliography

[1] D. Van Delft and P. Kes, "The discovery of superconductivity," *Physics Today*, vol. 63, no. 9, pp. 38–43, 2010.

[2] D. Van Delft, *Freezing Physics: Hieke Kamerlingh Onnes and the Quest for Cold*. Koninklijke Nederlandse Akademie van Wetenschappen, 2007.

[3] A. M. Forrest, "Meissner and ochsenfeld revisited," *European Journal of Physics*, vol. 4, no. 2, p. 117, 1983.

[4] W. Meissner and R. Ochsenfeld, "Ein neuer effekt bei eintritt der supraleitfähigkeit," *Naturwissenschaften*, vol. 21, no. 44, pp. 787–788, 1933.

[5] F. London and H. London, "The electromagnetic equations of the supraconductor," *Proceedings of the Royal Society of London. Series A-Mathematical and Physical Sciences*, vol. 149, no. 866, pp. 71–88, 1935.

[6] J. Schmalian, "Failed theories of superconductivity," *Modern Physics Letters B*, vol. 24, no. 27, pp. 2679–2691, 2010.

[7] J. Bardeen, L. N. Cooper, and J. R. Schrieffer, "Theory of superconductivity," *Physical Review*, vol. 108, no. 5, p. 1175, 1957.

[8] L. N. Cooper, "Bound electron pairs in a degenerate fermi gas," *Physical Review*, vol. 104, no. 4, p. 1189, 1956.

[9] M. Sigrist, "Introduction to unconventional superconductivity," in *AIP Conference Proceedings*, vol. 789, pp. 165–243, American Institute of Physics, 2005.

[10] M. Tinkham, *Introduction to superconductivity*. Courier Corporation, 2004.

[11] N. Ashcroft and N. Mermin, "Solid state physics (brooks cole, 1976)," *Cited on*, vol. 26, 1993.

[12] L. D. Landau and V. Ginzburg, "On the theory of superconductivity," *Zh. Eksp. Teor. Fiz.*, vol. 20, p. 1064, 1950.

[13] L. P. Gor'kov, "Microscopic derivation of the ginzburg-landau equations in the theory of superconductivity," *Sov. Phys. JETP*, vol. 9, no. 6, pp. 1364–1367, 1959.

[14] B. Josephson, "Possible new effect in superconducting tunneling," *Phys. Lett.*, vol. 1, pp. 251–253, 1962.

[15] S. Shapiro, "Josephson currents in superconducting tunneling: The effect of microwaves and other observations," *Physical Review Letters*, vol. 11, no. 2, p. 80, 1963.

[16] S. P. Benz and C. A. Hamilton, "Application of the josephson effect to voltage metrology," *Proceedings of the IEEE*, vol. 92, no. 10, pp. 1617–1629, 2004.

[17] J. Waldram and P. Wu, "An alternative analysis of the nonlinear equations of the current-driven josephson junction," *Journal of Low Temperature Physics*, vol. 47, no. 3, pp. 363–374, 1982.

[18] S.-O. Katterwe, *Properties of small $Bi_2Sr_2CaCu_2O_8$ intrinsic Josephson junctions: confinement, flux-flow and resonant phenomena*. PhD thesis, Department of Physics, Stockholm University, 2011.

[19] R. De Luca *et al.*, "Quantum interference in josephson junctions," *Journal of Modern Physics*, vol. 6, no. 05, p. 526, 2015.

[20] J. A. Blackburn, M. Cirillo, and N. Grønbech-Jensen, "A survey of classical and quantum interpretations of experiments on josephson junctions at very low temperatures," *Physics Reports*, vol. 611, pp. 1–33, 2016.

[21] J. E. Moore, "The birth of topological insulators," *Nature*, vol. 464, no. 7286, pp. 194–198, 2010.

[22] R. Snyder, C. Trimble, C. Rong, P. Folkes, P. Taylor, and J. Williams, "Weak-link josephson junctions made from topological crystalline insulators," *Physical Review Letters*, vol. 121, no. 9, p. 097701, 2018.

[23] T. H. Hsieh, H. Lin, J. Liu, W. Duan, A. Bansil, and L. Fu, "Topological crystalline insulators in the snte material class," *Nature Communications*, vol. 3, p. 982, 2012.

[24] A. Barone and G. Paterno, *Physics and applications of the Josephson effect*. Wiley, 1982.

[25] J. Williams, A. Bestwick, P. Gallagher, S. S. Hong, Y. Cui, A. S. Bleich, J. Analytis, I. Fisher, and D. Goldhaber-Gordon, "Unconventional josephson effect in hybrid superconductor-topological insulator devices," *Physical Review Letters*, vol. 109, no. 5, p. 056803, 2012.

[26] M. Veldhorst, M. Snelder, M. Hoek, T. Gang, V. Guduru, X. Wang, U. Zeitler, W. G. van der Wiel, A. Golubov, H. Hilgenkamp, *et al.*, "Josephson supercurrent through a topological insulator surface state," *Nature materials*, vol. 11, no. 5, p. 417, 2012.

[27] C. Kurter, A. Finck, Y. S. Hor, and D. J. Van Harlingen, "Evidence for an anomalous current–phase relation in topological insulator josephson junctions," *Nature communications*, vol. 6, p. 7130, 2015.

[28] J. B. Oostinga, L. Maier, P. Schüffelgen, D. Knott, C. Ames, C. Brüne, G. Tkachov, H. Buhmann, and L. W. Molenkamp, "Josephson supercurrent through the topological surface states of strained bulk hgte," *Physical Review X*, vol. 3, no. 2, p. 021007, 2013.

[29] K. Likharev, "Superconducting weak links," *Reviews of Modern Physics*, vol. 51, no. 1, p. 101, 1979.

[30] K. K. Likharev, *Dynamics of Josephson junctions and circuits.* Gordon and Breach Science Publishers, 1986.

[31] A. A. Golubov, M. Y. Kupriyanov, and E. Il'Ichev, "The current-phase relation in josephson junctions," *Reviews of modern physics*, vol. 76, no. 2, p. 411, 2004.

[32] E. M. Spanton, M. Deng, S. Vaitiekėnas, P. Krogstrup, J. Nygård, C. M. Marcus, and K. A. Moler, "Current–phase relations of few-mode inas nanowire josephson junctions," *Nature Physics*, vol. 13, no. 12, p. 1177, 2017.

[33] C. English, D. Hamilton, C. Chialvo, I. Moraru, N. Mason, and D. J. Van Harlingen, "Observation of nonsinusoidal current-phase relation in graphene josephson junctions," *Physical Review B*, vol. 94, no. 11, p. 115435, 2016.

[34] I. Sochnikov, L. Maier, C. A. Watson, J. R. Kirtley, C. Gould, G. Tkachov, E. M. Hankiewicz, C. Brüne, H. Buhmann, L. W. Molenkamp, *et al.*, "Nonsinusoidal current-phase relationship in josephson junctions from the 3d topological insulator hgte," *Physical Review Letters*, vol. 114, no. 6, p. 066801, 2015.

[35] "See supplemental material at http://link.aps.org/supplemental/10.1103/physrevlett.121.097701 for additional information on the material synthesis, device preparation, and additional data and simulations.,"

[36] P. Sessi, D. Di Sante, A. Szczerbakow, F. Glott, S. Wilfert, H. Schmidt, T. Bathon, P. Dziawa, M. Greiter, T. Neupert, *et al.*, "Robust spin-polarized midgap states at step edges of topological crystalline insulators," *Science*, vol. 354, no. 6317, pp. 1269–1273, 2016.

[37] N. Avraham, A. Norris, Y. Sun, Y. Qi, L. Pan, A. Isaeva, A. Zeugner, C. Felser, B. Yan, and H. Beidenkopf, "Coexisting surface states in the weak and crystalline topological insulator bi$_2$tei," *arXiv preprint arXiv:1708.09062*, 2017.

[38] C. Pauly, B. Rasche, K. Koepernik, M. Liebmann, M. Pratzer, M. Richter, J. Kellner, M. Eschbach, B. Kaufmann, L. Plucinski, *et al.*, "Subnanometrewide electron channels protected by topology," *Nature Physics*, vol. 11, no. 4, p. 338, 2015.

[39] C. Beenakker and H. Van Houten, "Josephson current through a superconducting quantum point contact shorter than the coherence length," *Physical Review Letters*, vol. 66, no. 23, p. 3056, 1991.

[40] H. Sellier, C. Baraduc, F. Lefloch, and R. Calemczuk, "Half-integer shapiro steps at the 0- π crossover of a ferromagnetic josephson junction," *Physical Review Letters*, vol. 92, no. 25, p. 257005, 2004.

[41] H. Sickinger, A. Lipman, M. Weides, R. Mints, H. Kohlstedt, D. Koelle, R. Kleiner, and E. Goldobin, "Experimental evidence of a φ josephson junction," *Physical Review Letters*, vol. 109, no. 10, p. 107002, 2012.

[42] C. T. Ke, C. M. Moehle, F. K. de Vries, C. Thomas, S. Metti, C. R. Guinn, R. Kallaher, M. Lodari, G. Scappucci, T. Wang, *et al.*, "Ballistic superconductivity and tunable π–junctions in insb quantum wells," *Nature Communications*, vol. 10, no. 1, pp. 1–6, 2019.

[43] Y. Tanaka, "Multicomponent superconductivity based on multiband superconductors," *Superconductor Science and Technology*, vol. 28, no. 3, p. 034002, 2015.

[44] Y. Yerin and A. Omelyanchouk, "Proximity and josephson effects in microstructures based on multiband superconductors," *Low Temperature Physics*, vol. 43, no. 9, pp. 1013–1037, 2017.

[45] Y. Tanaka and S. Kashiwaya, "Theory of josephson effects in anisotropic superconductors," *Physical Review B*, vol. 56, no. 2, p. 892, 1997.

[46] E. Il'Ichev, M. Grajcar, R. Hlubina, R. IJsselsteijn, H. Hoenig, H.-G. Meyer, A. Golubov, M. Amin, A. Zagoskin, A. Omelyanchouk, *et al.*, "Degenerate ground state in a mesoscopic $yba_2cu_3o_7$- x grain boundary josephson junction," *Physical Review Letters*, vol. 86, no. 23, p. 5369, 2001.

[47] F. Kidwingira, J. Strand, D. Van Harlingen, and Y. Maeno, "Dynamical superconducting order parameter domains in sr_2ruo_4," *Science*, vol. 314, no. 5803, pp. 1267–1271, 2006.

[48] E. Goldobin, D. Koelle, R. Kleiner, and A. Buzdin, "Josephson junctions with second harmonic in the current-phase relation: Properties of φ junctions," *Physical Review B*, vol. 76, no. 22, p. 224523, 2007.

[49] S. Frolov, D. Van Harlingen, V. Bolginov, V. Oboznov, and V. Ryazanov, "Josephson interferometry and shapiro step measurements of superconductor-ferromagnet-superconductor 0- π junctions," *Physical Review B*, vol. 74, no. 2, p. 020503, 2006.

[50] M. Moshe and R. Mints, "Shapiro steps in josephson junctions with alternating critical current density," *Physical Review B*, vol. 76, no. 5, p. 054518, 2007.

[51] F. Li, L. Wu, L. Chen, S. Zhang, W. Peng, and Z. Wang, "Measurement of the intrinsic higher harmonic current-phase relation in nbn/nicu/nbn josephson junctions," *Physical Review B*, vol. 99, no. 10, p. 100506, 2019.

[52] A. A. Reynoso, G. Usaj, C. Balseiro, D. Feinberg, and M. Avignon, "Spin-orbit-induced chirality of andreev states in josephson junctions," *Physical Review B*, vol. 86, no. 21, p. 214519, 2012.

[53] T. Yokoyama, M. Eto, and Y. V. Nazarov, "Anomalous josephson effect induced by spin-orbit interaction and zeeman effect in semiconductor nanowires," *Physical Review B*, vol. 89, no. 19, p. 195407, 2014.

[54] T. K. Ng and N. Nagaosa, "Broken time-reversal symmetry in josephson junction involving two-band superconductors," *EPL (Europhysics Letters)*, vol. 87, no. 1, p. 17003, 2009.

[55] S.-Z. Lin, "Josephson effect between a two-band superconductor with s++ or s±pairing symmetry and a conventional s-wave superconductor," *Physical Review B*, vol. 86, no. 1, p. 014510, 2012.

[56] V. G. Stanev and A. E. Koshelev, "Anomalous proximity effects at the interface of s-and s±-superconductors," *Physical Review B*, vol. 86, no. 17, p. 174515, 2012.

[57] A. Koshelev, "Phase diagram of josephson junction between s and s±superconductors in the dirty limit," *Physical Review B*, vol. 86, no. 21, p. 214502, 2012.

[58] I. B. Sperstad, J. Linder, and A. Sudbø, "Quantum transport in ballistic s±-wave superconductors with interband coupling: conductance spectra, crossed andreev reflection, and josephson current," *Physical Review B*, vol. 80, no. 14, p. 144507, 2009.

[59] Z. Huang and X. Hu, "Josephson effects in three-band superconductors with broken time-reversal symmetry," *Applied Physics Letters*, vol. 104, no. 16, p. 162602, 2014.

[60] Y. Asano, Y. Tanaka, M. Sigrist, and S. Kashiwaya, "Josephson current in s-wave-superconductor/sr_2ruo_4 junctions," *Physical Review B*, vol. 67, no. 18, p. 184505, 2003.

[61] Y. Asano, Y. Tanaka, M. Sigrist, and S. Kashiwaya, "Josephson interferometer in a ring topology as a proof of the symmetry of sr_2ruo_4," *Physical Review B*, vol. 71, no. 21, p. 214501, 2005.

[62] T. Nakamura, R. Nakagawa, T. Yamagishi, T. Terashima, S. Yonezawa, M. Sigrist, and Y. Maeno, "Topological competition of superconductivity in pb/ru/sr_2ruo_4 junctions," *Physical Review B*, vol. 84, no. 6, p. 060512, 2011.

[63] M. Anwar, R. Ishiguro, T. Nakamura, M. Yakabe, S. Yonezawa, H. Takayanagi, and Y. Maeno, "Multicomponent order parameter superconductivity of sr_2ruo_4 revealed by topological junctions," *Physical Review B*, vol. 95, no. 22, p. 224509, 2017.

[64] C. Trimble, M. Wei, N. Yuan, S. Kalantre, P. Liu, H.-J. Han, M.-G. Han, Y. Zhu, J. Cha, L. Fu, *et al.*, "Josephson detection of time-reversal symmetry broken superconductivity in snte nanowires," *NPJ Quantum Materials*, vol. 6, no. 1, pp. 1–6, 2021.

[65] C.-T. Chen, C. Tsuei, M. Ketchen, Z.-A. Ren, and Z. Zhao, "Integer and half-integer flux-quantum transitions in a niobium–iron pnictide loop," *Nature Physics*, vol. 6, no. 4, pp. 260–264, 2010.

[66] Y. Tanaka, H. Yamamori, T. Yanagisawa, T. Nishio, and S. Arisawa, "Experimental formation of a fractional vortex in a superconducting bi-layer," *Physica C: Superconductivity and its Applications*, vol. 548, pp. 44–49, 2018.

[67] X.-L. Qi, T. L. Hughes, and S.-C. Zhang, "Topological invariants for the fermi surface of a time-reversal-invariant superconductor," *Physical Review B*, vol. 81, no. 13, p. 134508, 2010.

[68] P. Hosur, X. Dai, Z. Fang, and X.-L. Qi, "Time-reversal-invariant topological superconductivity in doped weyl semimetals," *Physical Review B*, vol. 90, no. 4, p. 045130, 2014.

[69] Z. Guguchia, F. Von Rohr, Z. Shermadini, A. T. Lee, S. Banerjee, A. Wieteska, C. Marianetti, B. Frandsen, H. Luetkens, Z. Gong, *et al.*, "Signatures of the topological s+- superconducting order parameter in the type-ii weyl semimetal t d-$mote_2$," *Nature communications*, vol. 8, no. 1, pp. 1–8, 2017.

[70] P. Liu, Y. Xie, E. Miller, Y. Ebine, P. Kumaravadivel, S. Sohn, and J. J. Cha, "Dislocation-driven snte surface defects during chemical vapor deposition growth," *Journal of Physics and Chemistry of Solids*, vol. 128, pp. 351–359, 2019.

[71] J. Williams, A. Bestwick, P. Gallagher, S. S. Hong, Y. Cui, A. S. Bleich, J. Analytis, I. Fisher, and D. Goldhaber-Gordon, "Unconventional josephson effect in hybrid superconductor-topological insulator devices," *Physical Review Letters*, vol. 109, no. 5, p. 056803, 2012.

[72] S. Hart, H. Ren, T. Wagner, P. Leubner, M. Mühlbauer, C. Brüne, H. Buhmann, L. W. Molenkamp, and A. Yacoby, "Induced superconductivity in the quantum spin hall edge," *Nature Physics*, vol. 10, no. 9, pp. 638–643, 2014.

[73] K. Zuo, V. Mourik, D. B. Szombati, B. Nijholt, D. J. Van Woerkom, A. Geresdi, J. Chen, V. P. Ostroukh, A. R. Akhmerov, S. R. Plissard, *et al.*, "Supercurrent interference in few-mode nanowire josephson junctions," *Physical Review Letters*, vol. 119, no. 18, p. 187704, 2017.

[74] M. Weides, M. Kemmler, H. Kohlstedt, R. Waser, D. Koelle, R. Kleiner, and E. Goldobin, "0- π josephson tunnel junctions with ferromagnetic barrier," *Physical Review Letters*, vol. 97, no. 24, p. 247001, 2006.

[75] Y. Ishimaru, J. Wen, N. Koshizuka, and Y. Enomoto, "Superconducting-gap symmetry study using a/c boundary josephson junctions in $yba_2cu_3o_7$-δ stfilms," *Physical Review B*, vol. 55, no. 17, p. 11851, 1997.

[76] R. Rodríguez-Mota, E. Berg, and T. Pereg-Barnea, "Effects of order parameter self-consistency in a s±- s junction," *Physical Review B*, vol. 93, no. 21, p. 214507, 2016.

[77] J. Shen, Y. Jung, A. S. Disa, F. J. Walker, C. H. Ahn, and J. J. Cha, "Synthesis of snte nanoplates with {100} and {111} surfaces," *Nano Letters*, vol. 14, no. 7, pp. 4183–4188, 2014.

[78] J. Shen, Y. Xie, and J. J. Cha, "Revealing surface states in in-doped snte nanoplates with low bulk mobility," *Nano Letters*, vol. 15, no. 6, pp. 3827–3832, 2015.

[79] P. B. Allen and M. L. Cohen, "Carrier-concentration-dependent superconductivity in snte and gete," *Physical Review*, vol. 177, no. 2, p. 704, 1969.

[80] L. Brillson, E. Burstein, and L. Muldawer, "Raman observation of the ferroelectric phase transition in snte," *Physical Review B*, vol. 9, no. 4, p. 1547, 1974.

[81] K. Chang, J. Liu, H. Lin, N. Wang, K. Zhao, A. Zhang, F. Jin, Y. Zhong, X. Hu, W. Duan, *et al.*, "Discovery of robust in-plane ferroelectricity in atomic-thick snte," *Science*, vol. 353, no. 6296, pp. 274–278, 2016.

[82] K. Chang, B. J. Miller, H. Yang, H. Lin, S. S. Parkin, S. Barraza-Lopez, Q.-K. Xue, X. Chen, and S.-H. Ji, "Standing waves induced by valley-mismatched domains in ferroelectric snte monolayers," *Physical Review Letters*, vol. 122, no. 20, p. 206402, 2019.

[83] A. Bouhon and M. Sigrist, "Influence of the domain walls on the josephson effect in sr_2ruo_4," *New Journal of Physics*, vol. 12, no. 4, p. 043031, 2010.

[84] H. Kambara, S. Kashiwaya, H. Yaguchi, Y. Asano, Y. Tanaka, and Y. Maeno, "Anomalous transport through the p-wave superconducting channel in the 3-k phase of sr_2ruo_4," *Physical Review Letters*, vol. 101, no. 26, p. 267003, 2008.

[85] M. Anwar, T. Nakamura, S. Yonezawa, M. Yakabe, R. Ishiguro, H. Takayanagi, and Y. Maeno, "Anomalous switching in nb/ru/sr_2ruo_4 topological junctions by chiral domain wall motion," *Scientific Reports*, vol. 3, no. 1, pp. 1–6, 2013.

[86] I. T. Rosen, C. J. Trimble, M. P. Andersen, E. Mikheev, Y. Li, Y. Liu, L. Tai, P. Zhang, K. L. Wang, Y. Cui, M. A. Kastner, J. R. Williams, and D. Goldhaber-Gordon, "Fractional ac josephson effect in a topological insulator proximitized by a self-formed superconductor." `https://arxiv.org/abs/2110.01039`, 2021.

[87] L. Fu, C. L. Kane, and E. J. Mele, "Topological insulators in three dimensions," *Phys. Rev. Lett.*, vol. 98, p. 106803, Mar 2007.

[88] L. Fu and C. L. Kane, "Superconducting proximity effect and majorana fermions at the surface of a topological insulator," *Phys. Rev. Lett.*, vol. 100, p. 096407, Mar 2008.

[89] L. P. Rokhinson, X. Liu, and J. K. Furdyna, "The fractional ac josephson effect in a semiconductor–superconductor nanowire as a signature of majorana particles," *Nature Physics*, vol. 8, no. 11, pp. 795–799, 2012.

[90] D. Laroche, D. Bouman, D. J. van Woerkom, A. Proutski, C. Murthy, D. I. Pikulin, C. Nayak, R. J. van Gulik, J. Nygård, P. Krogstrup, *et al.*, "Observation of the 4π-periodic josephson effect in indium arsenide nanowires," *Nature Communications*, vol. 10, no. 1, pp. 1–7, 2019.

[91] J. Wiedenmann, E. Bocquillon, R. S. Deacon, S. Hartinger, O. Herrmann, T. M. Klapwijk, L. Maier, C. Ames, C. Brüne, C. Gould, *et al.*, "4 π-periodic josephson supercurrent in hgte-based topological josephson junctions," *Nature Communications*, vol. 7, no. 1, pp. 1–7, 2016.

[92] E. Bocquillon, R. S. Deacon, J. Wiedenmann, P. Leubner, T. M. Klapwijk, C. Brüne, K. Ishibashi, H. Buhmann, and L. W. Molenkamp, "Gapless andreev bound states in the quantum spin hall insulator hgte," *Nature Nanotechnology*, vol. 12, no. 2, pp. 137–143, 2017.

[93] R. S. Deacon, J. Wiedenmann, E. Bocquillon, F. Domínguez, T. M. Klapwijk, P. Leubner, C. Brüne, E. M. Hankiewicz, S. Tarucha, K. Ishibashi, H. Buhmann, and L. W. Molenkamp, "Josephson radiation from gapless andreev bound states in hgte-based topological junctions," *Phys. Rev. X*, vol. 7, p. 021011, Apr 2017.

[94] C. Li, J. C. de Boer, B. de Ronde, S. V. Ramankutty, E. van Heumen, Y. Huang, A. de Visser, A. A. Golubov, M. S. Golden, and A. Brinkman, "4π-periodic andreev bound states in a dirac semimetal," *Nature Materials*, vol. 17, no. 10, pp. 875–880, 2018.

[95] K. Le Calvez, L. Veyrat, F. Gay, P. Plaindoux, C. B. Winkelmann, H. Courtois, and B. Sacépé, "Joule overheating poisons the fractional ac josephson effect in topological josephson junctions," *Communications Physics*, vol. 2, no. 1, p. 4, 2019.

[96] P. Schüffelgen, D. Rosenbach, C. Li, T. W. Schmitt, M. Schleenvoigt, A. R. Jalil, S. Schmitt, J. Kölzer, M. Wang, B. Bennemann, *et al.*, "Selective area growth and stencil lithography for in situ fabricated quantum devices," *Nature Nanotechnology*, vol. 14, no. 9, pp. 825–831, 2019.

[97] D. Rosenbach, T. W. Schmitt, P. Schüffelgen, M. P. Stehno, C. Li, M. Schleenvoigt, A. R. Jalil, G. Mussler, E. Neumann, S. Trellenkamp, *et al.*, "Reappearance of first shapiro step in narrow topological josephson junctions," *Science Advances*, vol. 7, no. 26, p. eabf1854, 2021.

[98] J. Park, Y.-B. Choi, G.-H. Lee, and H.-J. Lee, "Characterization of shapiro steps in the presence of a 4π-periodic josephson current," *Phys. Rev. B*, vol. 103, p. 235428, Jun 2021.

[99] M. C. Dartiailh, J. J. Cuozzo, B. H. Elfeky, W. Mayer, J. Yuan, K. S. Wickramasinghe, E. Rossi, and J. Shabani, "Missing shapiro steps in topologically trivial josephson junction on inas quantum well," *Nature Communications*, vol. 12, no. 1, p. 78, 2021.

[100] B. Sacépé, J. B. Oostinga, J. Li, A. Ubaldini, N. J. G. Couto, E. Giannini, and A. F. Morpurgo, "Gate-tuned normal and superconducting transport at the surface of a topological insulator," *Nature Communications*, vol. 2, no. 1, p. 575, 2011.

[101] J. R. Williams, A. J. Bestwick, P. Gallagher, S. S. Hong, Y. Cui, A. S. Bleich, J. G. Analytis, I. R. Fisher, and D. Goldhaber-Gordon, "Unconventional josephson effect in hybrid superconductor-topological insulator devices," *Phys. Rev. Lett.*, vol. 109, p. 056803, Jul 2012.

[102] M. Veldhorst, M. Snelder, M. Hoek, T. Gang, V. K. Guduru, X. L. Wang, U. Zeitler, W. G. van der Wiel, A. A. Golubov, H. Hilgenkamp, and A. Brinkman, "Josephson supercurrent through a topological insulator surface state," *Nature Materials*, vol. 11, no. 5, pp. 417–421, 2012.

[103] C. Kurter, A. D. K. Finck, Y. S. Hor, and D. J. Van Harlingen, "Evidence for an anomalous current–phase relation in topological insulator josephson junctions," *Nature Communications*, vol. 6, no. 1, p. 7130, 2015.

[104] M. P. Stehno, V. Orlyanchik, C. D. Nugroho, P. Ghaemi, M. Brahlek, N. Koirala, S. Oh, and D. J. Van Harlingen, "Signature of a topological phase transition in the josephson supercurrent through a topological insulator," *Phys. Rev. B*, vol. 93, p. 035307, Jan 2016.

[105] S. Ghatak, O. Breunig, F. Yang, Z. Wang, A. A. Taskin, and Y. Ando, "Anomalous fraunhofer patterns in gated josephson junctions based on the bulk-insulating topological insulator bisbtese$_2$," *Nano Letters*, vol. 18, pp. 5124–5131, 08 2018.

[106] A. Q. Chen, M. J. Park, S. T. Gill, Y. Xiao, D. Reig-i Plessis, G. J. MacDougall, M. J. Gilbert, and N. Mason, “Finite momentum cooper pairing in three-dimensional topological insulator josephson junctions,” *Nature Communications*, vol. 9, no. 1, p. 3478, 2018.

[107] M. Kayyalha, A. Kazakov, I. Miotkowski, S. Khlebnikov, L. P. Rokhinson, and Y. P. Chen, “Highly skewed current–phase relation in superconductor–topological insulator–superconductor josephson junctions,” *npj Quantum Materials*, vol. 5, no. 1, p. 7, 2020.

[108] M. Bai, F. Yang, M. Luysberg, J. Feng, A. Bliesener, G. Lippertz, A. Taskin, J. Mayer, and Y. Ando, “Novel self-epitaxy for inducing superconductivity in the topological insulator $(\mathrm{bi}_{1-x}\mathrm{sb}_x)_2\mathrm{te}_3$,” *Physical Review Materials*, vol. 4, no. 9, p. 094801, 2020.

[109] H. Takayanagi, T. Akazaki, and J. Nitta, “Observation of maximum supercurrent quantization in a superconducting quantum point contact,” *Phys. Rev. Lett.*, vol. 75, pp. 3533–3536, Nov 1995.

[110] J. Xiang, A. Vidan, M. Tinkham, R. M. Westervelt, and C. M. Lieber, “Ge/si nanowire mesoscopic josephson junctions,” *Nature Nanotechnology*, vol. 1, no. 3, pp. 208–213, 2006.

[111] S. Abay, D. Persson, H. Nilsson, H. Xu, M. Fogelström, V. Shumeiko, and P. Delsing, “Quantized conductance and its correlation to the supercurrent in a nanowire connected to superconductors,” *Nano Letters*, vol. 13, no. 8, pp. 3614–3617, 2013.

[112] P. Krogstrup, N. Ziino, W. Chang, S. Albrecht, M. Madsen, E. Johnson, J. Nygård, C. M. Marcus, and T. Jespersen, “Epitaxy of semiconductor–superconductor nanowires,” *Nature Materials*, vol. 14, no. 4, pp. 400–406, 2015.

[113] M. Kjaergaard, H. J. Suominen, M. P. Nowak, A. R. Akhmerov, J. Shabani, C. J. Palmstrøm, F. Nichele, and C. M. Marcus, “Transparent semiconductor-superconductor interface and induced gap in an epitaxial heterostructure josephson junction,” *Phys. Rev. Applied*, vol. 7, p. 034029, Mar 2017.

[114] J. Zhang, C.-Z. Chang, Z. Zhang, J. Wen, X. Feng, K. Li, M. Liu, K. He, L. Wang, X. Chen, Q.-K. Xue, X. Ma, and Y. Wang, “Band structure engineering in $(\mathrm{bi}_{1x}\mathrm{sb}_x)_2\mathrm{te}_3$ ternary topological insulators,” *Nature Communications*, vol. 2, no. 1, p. 574, 2011.

[115] N. Koirala, M. Brahlek, M. Salehi, L. Wu, J. Dai, J. Waugh, T. Nummy, M.-G. Han, J. Moon, Y. Zhu, D. Dessau, W. Wu, N. P. Armitage, and S. Oh, “Record surface state mobility and quantum hall effect in topological insulator thin films via interface engineering,” *Nano Letters*, vol. 15, pp. 8245–8249, 12 2015.

[116] M. Salehi, H. Shapourian, I. T. Rosen, M.-G. Han, J. Moon, P. Shibayev, D. Jain, D. Goldhaber-Gordon, and S. Oh, "Quantum-hall to insulator transition in ultra-low-carrier-density topological insulator films and a hidden phase of the zeroth landau level," *Advanced Materials*, vol. 31, no. 36, p. 1901091, 2019.

[117] P. Schüffelgen, D. Rosenbach, E. Neumann, M. P. Stehno, M. Lanius, J. Zhao, M. Wang, B. Sheehan, M. Schmidt, B. Gao, *et al.*, "Stencil lithography of superconducting contacts on mbe-grown topological insulator thin films," *Journal of Crystal Growth*, vol. 477, pp. 183–187, 2017.

[118] J. Wang, A. M. DaSilva, C.-Z. Chang, K. He, J. K. Jain, N. Samarth, X.-C. Ma, Q.-K. Xue, and M. H. W. Chan, "Evidence for electron-electron interaction in topological insulator thin films," *Phys. Rev. B*, vol. 83, p. 245438, Jun 2011.

[119] I. T. Rosen, I. Yudhistira, G. Sharma, M. Salehi, M. Kastner, S. Oh, S. Adam, and D. Goldhaber-Gordon, "Absence of strong localization at low conductivity in the topological surface state of low-disorder sb_2te_3," *Physical Review B*, vol. 99, no. 20, p. 201101, 2019.

[120] S. Hikami, A. I. Larkin, and Y. Nagaoka, "Spin-Orbit Interaction and Magnetoresistance in the Two Dimensional Random System," *Progress of Theoretical Physics*, vol. 63, pp. 707–710, 02 1980.

[121] H. B. Michaelson, "The work function of the elements and its periodicity," *Journal of Applied physics*, vol. 48, no. 11, pp. 4729–4733, 1977.

[122] D. Takane, S. Souma, T. Sato, T. Takahashi, K. Segawa, and Y. Ando, "Work function of bulk-insulating topological insulator $bi_{2-x}sb_xte_{3-y}se_y$," *Applied Physics Letters*, vol. 109, no. 9, p. 091601, 2016.

[123] G. E. Blonder, M. Tinkham, and T. M. Klapwijk, "Transition from metallic to tunneling regimes in superconducting microconstrictions: Excess current, charge imbalance, and supercurrent conversion," *Phys. Rev. B*, vol. 25, pp. 4515–4532, Apr 1982.

[124] H. Courtois, M. Meschke, J. T. Peltonen, and J. P. Pekola, "Origin of hysteresis in a proximity josephson junction," *Phys. Rev. Lett.*, vol. 101, p. 067002, Aug 2008.

[125] A. Y. Kitaev, "Unpaired majorana fermions in quantum wires," *Physics-Uspekhi*, vol. 44, no. 10S, p. 131, 2001.

[126] L. Fu and C. L. Kane, "Josephson current and noise at a superconductor/quantum-spin-hall-insulator/superconductor junction," *Physical Review B*, vol. 79, no. 16, p. 161408, 2009.

[127] R. M. Lutchyn, J. D. Sau, and S. D. Sarma, "Majorana fermions and a topological phase transition in semiconductor-superconductor heterostructures," *Physical Review Letters*, vol. 105, no. 7, p. 077001, 2010.

[128] C. Kane and F. Zhang, "The time reversal invariant fractional josephson effect," *Physica Scripta*, vol. 2015, no. T164, p. 014011, 2015.

[129] H.-J. Kwon, K. Sengupta, and V. M. Yakovenko, "Fractional ac josephson effect in p-and d-wave superconductors," *The European Physical Journal B-Condensed Matter and Complex Systems*, vol. 37, no. 3, pp. 349–361, 2004.

[130] A. De Cecco, K. Le Calvez, B. Sacépé, C. B. Winkelmann, and H. Courtois, "Interplay between electron overheating and ac josephson effect," *Phys. Rev. B*, vol. 93, p. 180505, May 2016.

[131] C. D. Shelly, P. See, I. Rungger, and J. M. Williams, "Existence of shapiro steps in the dissipative regime in superconducting weak links," *Phys. Rev. Applied*, vol. 13, p. 024070, Feb 2020.

[132] P.-M. Billangeon, F. Pierre, H. Bouchiat, and R. Deblock, "ac josephson effect and resonant cooper pair tunneling emission of a single cooper pair transistor," *Phys. Rev. Lett.*, vol. 98, p. 216802, May 2007.

[133] F. Domínguez, F. Hassler, and G. Platero, "Dynamical detection of majorana fermions in current-biased nanowires," *Phys. Rev. B*, vol. 86, p. 140503, Oct 2012.

[134] D. Averin and A. Bardas, "ac josephson effect in a single quantum channel," *Phys. Rev. Lett.*, vol. 75, pp. 1831–1834, Aug 1995.

[135] S. R. Mudi and S. M. Frolov, "Model for missing shapiro steps due to bias-dependent resistance," 2021.

[136] P. F. Bagwell, "Suppression of the josephson current through a narrow, mesoscopic, semiconductor channel by a single impurity," *Phys. Rev. B*, vol. 46, pp. 12573–12586, Nov 1992.

[137] K. Ueda, S. Matsuo, H. Kamata, Y. Sato, Y. Takeshige, K. Li, L. Samuelson, H. Xu, and S. Tarucha, "Evidence of half-integer shapiro steps originated from nonsinusoidal current phase relation in a short ballistic inas nanowire josephson junction," *Phys. Rev. Research*, vol. 2, p. 033435, Sep 2020.